Politecnico di Torino

Master’s degree in Aerospace Engineering

Master Thesis

Liner Optimization for Fan Noise Reduction

Supervisors:
Prof. Francesco Avallone
Ing. Francesco Paolo Adamo
Ing. Mattia Barbarino
Ing. Francesco Petrosino

Candidate: Dario Antonio Orlando

April 2024

Ringraziamenti

Desidero esprimere la mia più profonda gratitudine al Professor Francesco Avallone, mio relatore di tesi, per la sua guida nella risoluzione dei problemi e il suo aiuto costante. La sua profonda esperienza e conoscenza nell'ambito dell'aeroacustica sono stati fondamentali per lo sviluppo e il completamento di questa tesi. La sua dedizione, la sua competenza e la profonda stima che hanno i colleghi di lui sono qualcosa che, aldilà di quale sarà il mio percorso, aspiro a raggiungere.

Un sentito ringraziamento va inoltre ai ricercatori del Centro Italiano di Ricerche Aerospaziali (CIRA) Francesco Adamo (mio referente all'esterno del Politecnico di Torino), Mattia Barbarino e Francesco Petrosino per il loro prezioso sostegno, orientamento e competenza durante lo svolgimento della mia tesi. I loro contributi e il loro aiuto sono stati fondamentali nel direzionare il progetto e nell'ottenimento dei risultati.

Abstract

Aviation has become increasingly integral to modern society over the years, addressing daily the needs of millions of travelers worldwide. However, this comes with a significant environmental cost, including noise emissions. High noise emissions have important implications for the health, leading to issues such as insomnia and consequently contributing to cardiovascular diseases. This has led institutions to develop increasingly stringent regulations for noise pollution control in the vicinity of airports, giving rise to new challenges in ensuring compliance with acoustic reduction standards.

Acoustic liners are an important ally in noise reduction, allowing to comply with the regulatory limit. The simpler acoustic liners (single-degree-of-freedom) can be compared to a Helmholtz Resonator, which is capable of absorbing a portion of the acoustic energy and dissipating it through fluid dynamic viscous components. By calibrating the geometric dimensions of the Helmholtz Resonator, it is possible to achieve the desired resonance frequency at which the attenuation is maximum. However, shifting towards ultra-high bypass ratio turbofan engines to allow for increased efficiency results in a lower fan rotation speed, leading to a lower-frequency and broader acoustic emission spectrum, and thus making traditional acoustic liners less effective: lower attenuation frequencies require greater liner depths, this conflicting with the need for slimmer nacelles due to the significant increase in their diameter to achieve ever higher bypass ratios. Additionally, broadband attenuation must be ensured. Hence, the need to develop new liner geometries and models emerged, along with the necessity for methods that enable determining the geometric parameters of the liner that best allow compliance with regulations at certification points.

This thesis presents an optimization code developed in Python that, coupled with the aeroacoustic calculation software Actran, allows for the definition of geometric parameters of the acoustic liner, such as cavity depth and dia-

meter of the orifices, ensuring minimal acoustic emission in the far field. In doing so, the most suitable semi-empirical models for liner's response have been chosen, where the liner's response depends precisely on the geometric parameters to be optimized. In particular, the use of both single-degree-of-freedom and two-degree-of-freedom semi-empirical liner models allowed for evaluating how much the noise was attenuated depending on the type of liner used compared to the case without acoustic treatment. Subsequently, the attenuation achieved was also compared for cases of absence of flow, uniform flow, and non-uniform flow. To determine the best optimization approach, the results obtained were compared using both local optimization algorithms and global optimization algorithms, before leaning towards a sequential use of the two.

This optimization approach has thus resulted in an improvement of more than 10 dB for both SDOF and DDOF compared to the scenario of a non-optimized liner. The sequential use of a global and a local optimizer proved effective for more complex semi-empirical models, where finding the minimum is more challenging. Conversely, for simpler liner models, employing a global optimizer alone proved sufficient, ensuring significantly reduced computational times. Additionally, the presence of airflow was found not to impact the optimal point itself but rather the value of acoustic emission at the optimal point. Therefore, the optimization framework developed represents a valuable tool for maximizing available technology to meet regulatory requirements.

Contents

List of Figures

List of Tables

Chapter 1

Introduction

Aviation has become increasingly integrated to modern society over the years, addressing daily the needs of millions of travelers worldwide. However, this comes with a significant environmental cost, including pollutants and greenhouse gas emissions, as well as noise emissions [30]. High noise emissions have important implications for the health, leading to issues such as insomnia and consequently contributing to cardiovascular diseases [8]. This has led the International Civil Aviation Organization (ICAO) to develop increasingly stringent regulations for noise pollution control in the vicinity of airports (figure 1.1) [14], giving rise to new challenges in ensuring compliance with new acoustic reduction standards.
The noise produced by an aircraft has two main contributions: the airframe and the engine. The first is primarily due to the landing gear, flaps, and

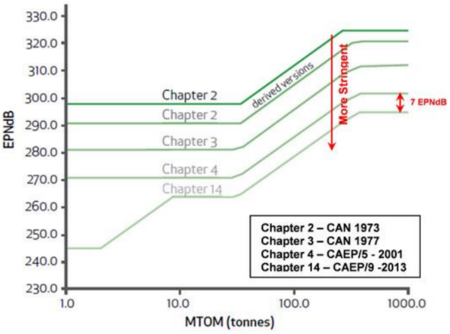

Figure 1.1: Historical trend of maximum EPNLs (in EPNdB) through the revisions of Annex 16 [13]

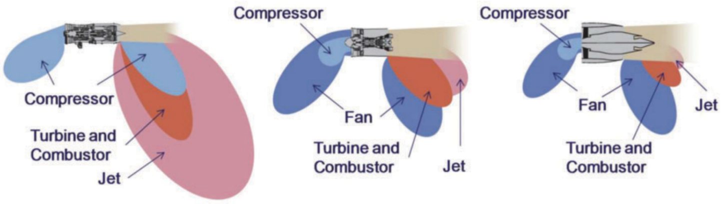

Figure 1.2: Noise changes with increasing turbofan engine bypass. [42]

slats, while the second, typically dominant and therefore more significant for certification purposes, is caused by the jet and the fan. Jet noise is associated with the high-velocity exhaust gases exiting the engine nozzle, while fan noise is a result of the interaction of the blades with the turbulent airflow [30].

Shifting towards ultra-high by-pass ratio (BPR) turbofan allows for increased efficiency by lowering fuel consumption. However, this has an impact on the acoustic emissions of the engine (figure 1.2) now primarily attributed to the fan noise rather than the jet noise: an increase in the by-pass ratio leads to a reduction in the exhaust gas velocities, making it possible to comply with regulations [42]. On the other side, a higher BPR results in a lower fan rotation speed, leading to a lower-frequency and broader acoustic emission spectrum. This shift makes it more challenging to mitigate the noise produced by the fan, which now plays a primary role. Moreover, mitigating fan noise is a complex challenge due to its multiple origins. The emission spectrum includes both tonal components at multiples of the blade passing frequency and a broadband component resulting from the interaction of turbulent flow with blades and mainly vanes because of the fan wake (figure 1.3) [21].

Acoustic liners are an important ally in noise reduction, allowing to comply with the regulatory limit. The changes mentioned above, however, give rise to several new challenges: lower attenuation frequencies require greater liner depths, this conflicting with the need for slimmer nacelles due to the significant increase in their diameter to achieve ever higher Bypass Ratios [43]. Additionally, broadband attenuation must be ensured [34]. Hence, the need to develop new liner geometries and models emerged, along with the necessity for methods that enable determining the geometric parameters of the liner that best allow compliance with regulations at certification points.

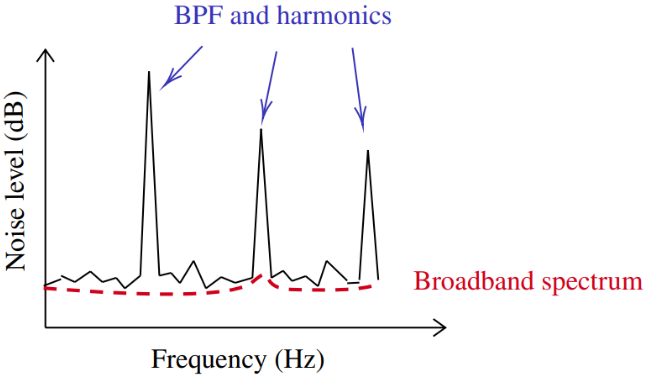

Figure 1.3: Example of noise spectrum from a subsonic fan. [30]

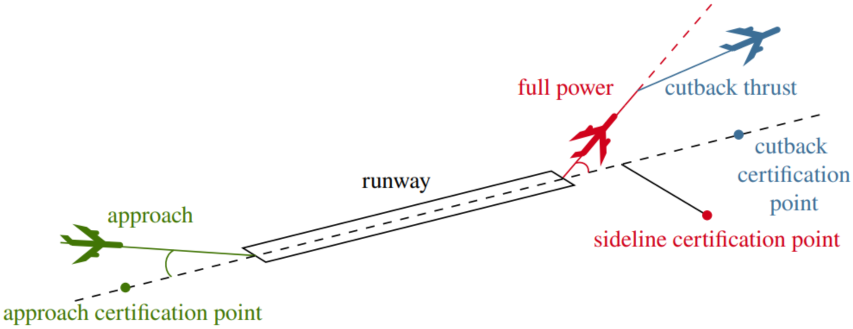

Figure 1.4: Noise changes with increasing turbofan engine bypass. [30]

In particular, ICAO has defined the maximum noise levels an aircraft can generate at specific certification points (figure 1.4) [30]:

- **Take-off sideline configuration:** in this take-off phase, the engine is at maximum power, and the produced noise is at its maximum.

- **Take-off cutback configuration:** in this take-off phase, the engine is at reduced power, this scenario represents the minimum noise perceived during a take-off operation.

- **Approach configuration:** this condition represents the noise perceived during the final approach phase.

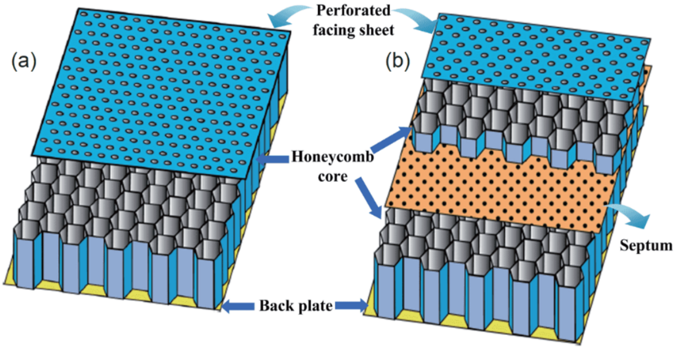

Figure 1.5: Schematics of basic structures of (a) SDoF and (b) DDoF liners [29]

1.1 Acoustic Liners

Various types of acoustic liners exist, ranging from the simplest Single Degree of Freedom (SDoF) to the most innovative meta-acoustic ones.

SDoF liners are the cheapest and easiest to manufacture. They are composed of a rigid honeycomb core with a perforated plate on top (figure 1.5), capable of both enhancing absorption and maintaining the flow as orderly as possible on the inner wall of the nacelle [33], and a rigid back plate on the opposite side. Their behavior is similar to that of a Helmholtz resonator, with an absorption peak at the resonance frequency, that depends on the depth of the honeycomb core (deeper liners result in a lower resonance frequency), and a relatively narrow absorption spectrum. The perforate facesheet can be characterized by: percentage open area (POA σ), hole diameter (d) and thickness (t), honeycomb core by its depth (h). The cell size is chosen so that the liner can be considered locally reacting [42]. It is possible to modify these geometric parameters to optimize the performance of the liner and ensure compliance with regulations [33]. Zandbergen [43] defined a liner as locally reacting (figure 1.6) if its local response is dependent only upon the local acoustic pressure, if only plane wave can propagate the liner can be considered local-reacting, otherwise its response would also depend on the angle of incidence of the acoustic wave on the liner [22]. Liners are local-reacting only if theirs cells are acoustically isolated from each other, the presence of drainage slots for safety reasons actually makes most acoustic liners non-locally reacting, allowing the propagation of acoustic waves

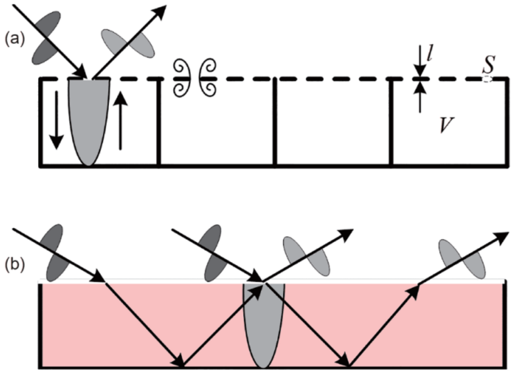

Figure 1.6: Schematics of (a) local-reacting liner and (b) bulk-reacting liner. [29]

parallel to the surface of the liner between two adjacent cavities. If the cell width of an acoustic liner is allowed to increase, additional cross-modes may propagate at higher frequencies, and the liner response subsequently becomes a function of the incident mode angle, rendering the liner non-locally reacting. Bulk-reacting liners, such as liners with facing sheets backed by resistive foams or packed fibers, are also known as non-locally reacting liners [43]. Gravagnone et al [22] performed a parametric study showing a gain in insertion loss for non-locally reacting liners with porous cell walls or wide cell (where also cross modes are cut-on) in comparison with local-reacting ones, with a broader absorption spectrum. This occurs because multi-modal sound arriving on these liner types at differing propagation angles will travel within the bulk material at non-normal angles, with varying path lengths, permitting these liner types to be optimized to provide absorption over a relatively large frequency range [43]. Despite this broader absorption spectrum, they are not used in aircraft engines due to their tendency to retain fluid.

Double Degree of Freedom (DDoF) liners (figure 1.5) meet the requirements of broadening the absorption band thanks to a dual absorption peak, as demanded by ultra high bypass ratio engines, with the constraint of a narrower nacelle. They are geometrically very similar to SDoF liners but with a second honeycomb core, separated from the first by an intermediate resistive sheet, also known as a septum [14], resulting in increased complexity and weight of the structure.

In recent years, new designs with complex cavities have been studied to max-

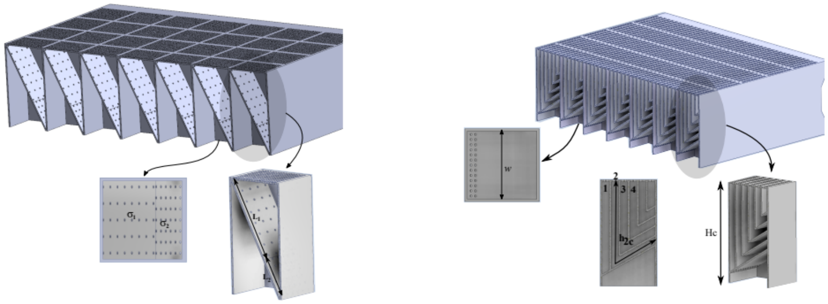

(a) Slanted Septum Core with variable open area

(b) MultiFOCAL Panel

Figure 1.7: Schematics of the Slanted Septum Core (SSC) and the Multi-FOCAL liner concepts. [34]

imize noise reduction at low frequencies while maintaining an acceptable structural size. Sugimoto [37] has demonstrated that the inclusion of folded cavities is effective in reducing noise simultaneously at medium and low frequencies. The use of folded cavities allows for greater depth compared to traditional straight cavities while utilizing the same space. At low frequencies, the acoustic wave propagating through the face sheet turns the corner and propagates as if it does not 'see' the fold. At high frequencies, the wave is mostly reflected from the fold. Therefore, this folded cavity behaves as a deeper cavity at low frequencies and as a shallow cavity for high frequencies [15]. Palani et al [34] evaluated the attenuation performances of two novel liners: one with a slanted septum core with varying percentage open area to increase the propagation path length for low frequency waves [15], the other a multiple folded cavity acoustic liner (figure 1.7). The computational model was based on the geometry of the Royal Netherlands Aerospace Centre (NLR) flow duct facility, test was performed under grazing flow and in the presence of high intensity sound waves using COMSOL and assuming equal energy per mode distribution. Both geometries have shown an enlargement of the attenuation band, while maintaining a smaller dimension compared to SDoF, with a significant increase in insertion loss, especially at frequencies below 1.2 kHz, where the insertion loss $IL = \Delta_{PWL}^{withliner} - \Delta_{PWL}^{withoutliner}$ is the difference between the sound power transmission loss with and without the liner. Broadband attenuation with reduced space requirements can also be achieved through the use of variable-length liners (figure 1.8). However, the production of these liners with complex geometries such as folded, slanted,

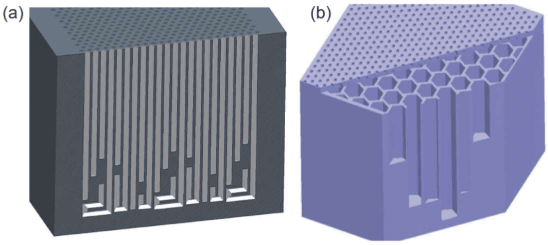

Figure 1.8: Schematics of two types of variable-depth liners with (a) narrow chamber and (b) wide chamber. [29]

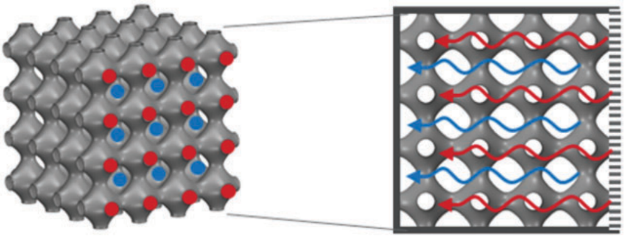

Figure 1.9: Example of meta-acoustic liner design. [42]

or multi-depth liners is complex to execute and is not possible with traditional manufacturing methods. Therefore, it requires the use of additive manufacturing [15].

The most innovative frontiers for acoustic attenuation involve the use of metamaterials (figure 1.9), which can be defined as a macroscopic composite of periodic or non-periodic structure, whose function is due to both the cellular architecture and the chemical composition [29]. These structures contain interconnected air volume cells with a large number of degrees of freedom, enabling attenuation across a lower and broader frequency range while still fitting within a compact space. Beck et al. [6] have demonstrated that the absorption coefficient for these liners can be up to 10 times higher than that of traditional honeycomb ones at the designed resonance frequency. The introduction of new materials also allows placing the liners not only near the fan inlet or along the exhaust bypass duct (figure 1.10), where they are typically inserted, but also in high-temperature areas, opening up new noise reduction scenarios.

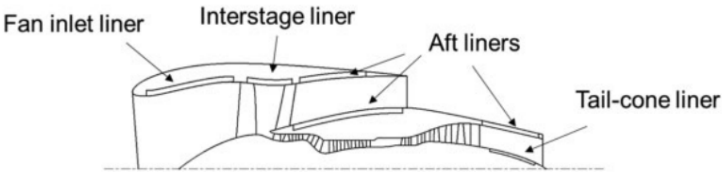

Figure 1.10: Typical placement of acoustic treatment inside an engine and nacelle. [42]

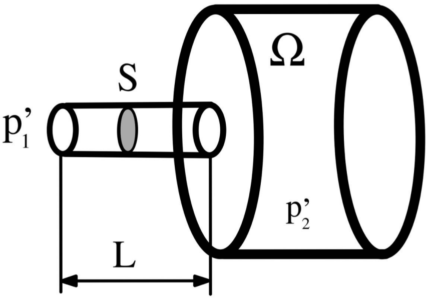

Figure 1.11: Helmholtz Resonator scheme

1.1.1 Helmholtz Resonator

SDoF acoustic liner can be compared to an Helmholtz resonator; it is capable of absorbing a portion of the acoustic energy and dissipating it through fluid dynamic components. More precisely: the perturbation p_1' is applied at one end of the duct with length L and cross-sectional area A (figure 1.11), which opens into the volume Ω where the fluid is at rest and where the induced oscillations p_2' and ρ_2' are uniform [5].
p_1' generates a flow rate Q in Ω:

$$Q = \Omega \frac{\partial^2 \rho_2'}{\partial t^2} \tag{1.1}$$

Assuming small, harmonic oscillations $\rho_2' = \hat{\rho}_2 e^{i\omega t}$ and $Q = \hat{Q} e^{i\omega t}$

$$\hat{Q} = i\omega\Omega\hat{\rho}_2 \tag{1.2}$$

$$\hat{\rho}_2 = \frac{\hat{Q}}{i\omega\Omega} \tag{1.3}$$

$$\hat{p}_2 = c_0^2 \hat{\rho}_2 = \frac{c_0^2 \hat{Q}}{i\omega\Omega}$$

Writing the momentum balance in the duct in the case of incompressibility:

$$-\frac{1}{\rho_0}\frac{p_2' - p_1'}{L} = \frac{\partial u'}{\partial t} \tag{1.4}$$

for harmonic oscillation and using the the derived formula for $\hat{p}_2$

$$-\frac{1}{\rho_0}\frac{\hat{p}_2 - \hat{p}_1}{L} = i\omega\hat{u} = i\frac{\omega\hat{Q}}{\rho_0 S} \tag{1.5}$$

$$\hat{p}_1 = \hat{p}_2 + i\omega\frac{L\hat{Q}}{S} = (\frac{c_0^2}{i\omega\Omega} + i\omega\frac{L}{S})\hat{Q} = = i(\omega^2 - \frac{c_0^2 S}{\Omega L})\frac{\hat{Q}L}{\omega S} = i(\omega^2 - \omega_R^2)\frac{\hat{Q}L}{\omega S} \tag{1.6}$$

$$\hat{p}_1 = i(\omega^2 - \omega_R^2)\frac{\hat{Q}L}{\omega S} \tag{1.7}$$

$\hat{p}_1$ is a small but finite value; consequently, as ω approaches the resonance frequency, the multiplicative flow term must increase significantly. This can be interpreted as the action of a fluid piston in duct causing large oscillations $\hat{p}_2$. The presence of large gradients in a viscous flow results in dissipation, whose effect is small enough to damp amplitudes only on the order of acoustic oscillations. By calibrating the geometric dimensions of the Helmholtz Resonator, it is possible to achieve the desired resonance frequency. This is where the idea of acoustic liners originates. More specifically, acoustic energy is converted into rotational kinetic energy in the form of vortex shedding and dissipated through viscous effects due to the shear layer close to the wall of the cavity. [35].

1.1.2 Impedance

A liner is characterized in terms of acoustic impedance Z, which is defined in the frequency domain as the ratio of the acoustic pressure and normal acoustic velocity [44]:

$$Z = \frac{\hat{p}}{\hat{u}_n} \tag{1.8}$$

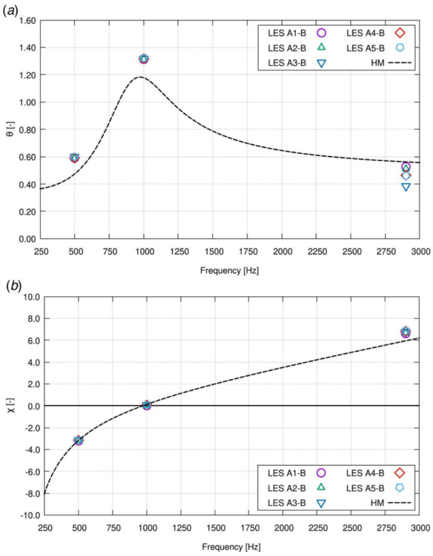

Figure 1.12: Effect of the frequency on the SDoF cell: (a) resistance and (b) reactance. [20]

where $\hat{p}$ and $\hat{u}_n$ are the Fourier coefficients of the pressure and normal velocity. Normalizing by the medium's characteristic impedance $\rho_0 c_0$, normalized acoustic impedance $z = \theta + i\chi$ is obtained, where θ is the normalized resistance θ and χ the normalized reactance. Resistance represents the real part of impedance and describes the dissipation of acoustic energy. If it has a positive value, energy is being dissipated; otherwise, it would be produced. Reactance is a phase and represents the imaginary component of impedance that provides the frequency at which resonance occurs for a given geometry, corresponding to the frequency at which reactance equals zero. Under resonance conditions an absorption peak is expected due to the cancellation of the reactance and the maximization of the resistance, leading to a local minimum in the acoustic impedance of the system (figure 1.12) [20]. This is definitely true in the absence of grazing flow, whose presence tends to slightly shift the frequency at which resonance occurs, because both resistance and reactance are influenced by the presence of grazing flow (the flow that runs along the liner) and bias flow (typically absent, flows in cavities for high-temperature material survival) (figure 1.13).

To obtain an accurate description of the liner's behavior, it is therefore crucial to have a precise description of the fluid dynamic field and its interaction

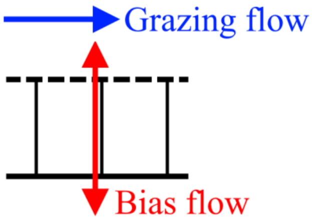

Figure 1.13: Grazing and bias flow for SDoF liner. [7]

with the acoustic one. Firstly because, as seen, ”the conversion of acoustic energy into rotational kinetic energy represents the dominant mechanism for noise reduction” [35]. Tam et al. [40] performed a 2D Direct Numerical Simulation (DNS), showing that this holds true both in the absence and presence of grazing flow. However, in the latter case, it was shown that ”the large-scale vortices, ejected from the resonator’s orifice, are advected by the grazing flow and interact with downstream cavities”, especially in the presence of high SPL incident waves. It is also very important to have a good representation of the the counter-rotating vortices that form upstream of the liner (and thus of the fluid dynamics in this region) since they, by obstructing part of the passage, reduce the perceived cavity area, increasing resistance [35] (figure 1.14). This recirculation region within the orifice is quasi-steady, because it slightly oscillates within the orifice [17] and is caused by the interaction of the turbulent flow with the orifice itself and affects the interaction of the acoustic wave with the liner. In addition to these vortices within the orifice, figure 1.14 also shows the clockwise circulation region within the cavity, which is the main cause of viscous dissipation in the liner. Furthermore, the behavior of the vortices deep inside the cavities tends to be somewhat random.

However, the evaluation of impedance in the presence of flow still poses a challenge. Indeed, by performing a numerical evaluation with flow the calculated impedance value show gap compared to experimental data, particurarly with respect to the resistance values (figure 1.15). This is because the physics behind the interaction between the acoustic field and the turbulent flow is still not fully understood, and it remains a research topic [35]. Another important aspect contributing to the difference between numerically and experimentally obtained results, currently under careful evaluation, is the discrepancy between simulated and experimental geometries. This is

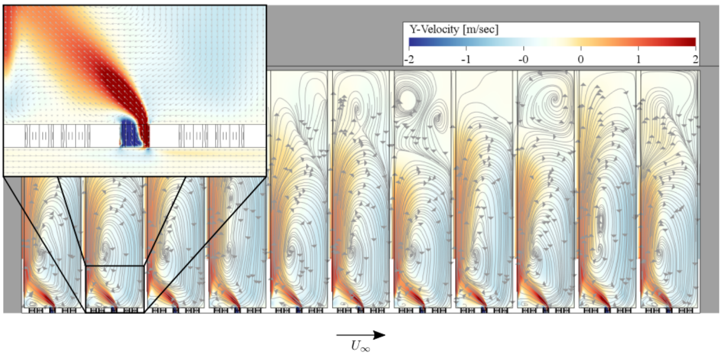

Figure 1.14: Contour plot of the y velocity component of the flow, streamlines inside the cavities and detailed near orifice velocity vectors. [35]

influenced by a series of inaccuracies and defects arising from the manufacturing process of the liners, particularly concerning the roundness of cavity edges, which are imprecise and not perfectly circular. Considering that these imperfections exist in millimeter-sized holes, they can significantly alter the liner's response. Palani et al. [34] also studied the effect of mean flow in term of boundary layer velocity profile and thickness on optimal impedance evaluation, a quarter-sine profile and a 1/4th power-law profile were evaluated (figure 1.16). The computational model is based on the geometry of the Royal Netherlands Aerospace Centre (NLR) flow duct facility and the Linearised Euler Equations (LEE) frequency domain model in COMSOL is used to describe the propagation of the sound field within the duct. The results demonstrated a dependence of the optimal impedance on the Mach number and the shape of the velocity profile (figure 1.17), due to the different refraction effect caused by the presence of a velocity gradient in the boundary layer zone.

1.1.3 Impedance Evaluation

Winkler et al [42] provided an overview of the main methods for impedance evaluation. DNS are the gold standard, and with Large Eddy Simulations (LES) and the Boltzmann Lattice Method (BLM), they fall into the category of high-fidelity methods. High fidelity simulations direct resolve liner perforation and geometry details using a numerical grid and, there is the need of this method in presence of unsteady flow, high acoustic amplitudes, for

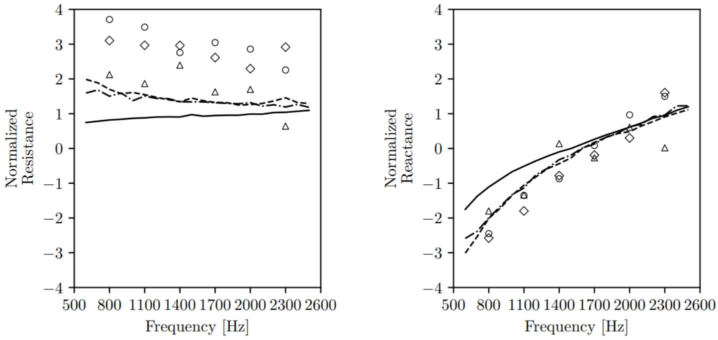

Figure 1.15: Normalized impedance for the M=0.3 grazing flow case as a function of the incident acoustic wave frequency (downstream source): (–) experimental [in-situ]; (- -) experimental [MM]; (-·-) experimental [KT]; (△) numerical [in-situ]; (○) numerical [MM]; (◇) numerical [KT]. [35]

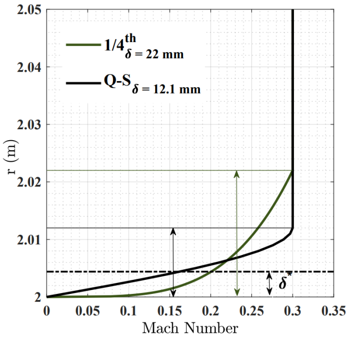

Figure 1.16: 1/4th power-law, and quarter-sine. [34]

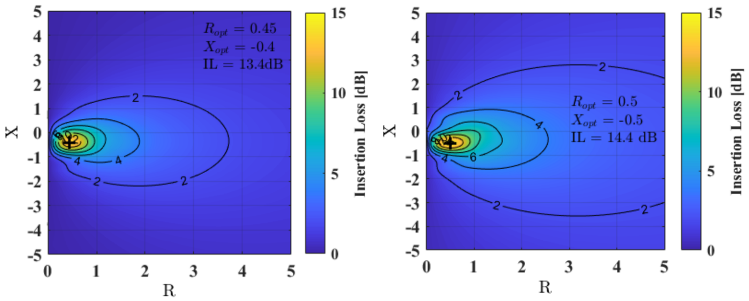

(a) Uniform flow M = +0.3 **(b) 1/4th Power-law M = +0.3**

Figure 1.17: 1/4th power-law, and quarter-sine. [34]

advanced liner design and for explore in detail a small number of facesheet holes and a single cavity. These methods allow for a more in-depth focus on exploring the physics of both traditional and more advanced liners, especially concerning the transfer of energy from the acoustic component to vortex motion. LBM VLES [35] maintains good fidelity but with a lower computational cost compared to DNS, but not low enough to include it in the design process. These simulations are considered very promising, especially due to their low numerical dissipation. However, being a relatively new method, the number of studies on this topic is still limited [42]. Mid-fidelity methods instead solve wave equation with embedded sub-models for perforations, or Linearized Eulerian Equation (LEE), commercial software like COMSOL or Actran follow these approaches. These tools are capable of either using an impedance boundary condition to represent the liner or a simplified sub-model to capture the leading-order acoustic effects of facesheet and septum perforations by modeling them as a transfer impedance within the fluid domain, with empirically determined parameters. Comparisons to experimental data have shown that these tools can be used with confidence [42].

1.2 Impedance Models

One of the most critical aspects is the development and evaluation of new models that can be integrated into the acoustic liner design process. Indeed, these models often fail in modeling innovative geometries that deviate from the more conventional SDoF or DDoF liner designs. However, reduced-order models (ROM) allow for achieving good results in the modeling of traditional liners, with lower computational costs compared to Actran and COMSOL and high-fidelity methods, although they represent fewer details. because of this, despite the development of many semi-empirical models over the years, different models applied to the same geometry can yield varying results when diverging from more conventional geometries.

1.2.1 Goodrich Model

A valid ROM for SDoF impedance prediction is the Goodrich Model, obtained by appropriately modifying the Crandall's solution. The normalized

Table 1.1: Geometric characteristic of Liners

Configuration	1	2
POA(%)	6.4	15.0
Hole Diameter (mm)	0.99	0.99
Sheet Thickness (mm)	0.64	0.64
Cavity Depth (mm)	38.1	38.1

impedance $z = \theta + i\chi$ is divided in three main contributes:

$$z = (\theta_l + \theta_{nl} + \theta_{gf}) + i(\chi_l + \chi_{nl} + \chi_{gf}) \tag{1.9}$$

where l indicates a linear term associated with the viscous flow through the orifices, nl a non-linear term associated with high amplitude acoustic waves leading to the formation of a jet flow through the orifices with vortex ring generation and turbulence breakdown and gf a linear term accounting for the effect of the grazing flow over the facesheet.
Winkler et al [42] compared the results obtained with LBM VLES, Goodrich Model, and experimental approach with no flow and in presence of grazing and bias flow. Simulations are performed for the NASA Langley Research Center's (LaRC) Normal Incidence Tube (NIT) and Grazing Flow Impedance Tube (GFIT) setups and the results are compared to available NASA experimental data and to Goodrich model. The simulations are performed with the LBM code PowerFLOW. Two configuration of SDoF liners were studied (table: 1.1). Acoustic waves consisting of a broadband source from 50 Hz to 5 kHz and OASPL of 130 dB are injected upstream of the SDoF liner.

Without Flow

In the absence of flow, only the first term of the Goodrich model remains:

$$\begin{aligned} z_l = {} & \frac{8\mu t}{\rho c \sigma a^2}\left(\sqrt{1+\frac{(k_s a)^2}{32}} + \frac{\sqrt{2}k_s a^2}{2t}\right) + \\ & + i\left\{\frac{\omega t}{c\sigma}\left[1+\left(9+\frac{(k_s a)^2}{2}\right)^{-0.5} + 2\frac{8a}{3\pi t}\right] - cot(kh)\right\} \end{aligned} \tag{1.10}$$

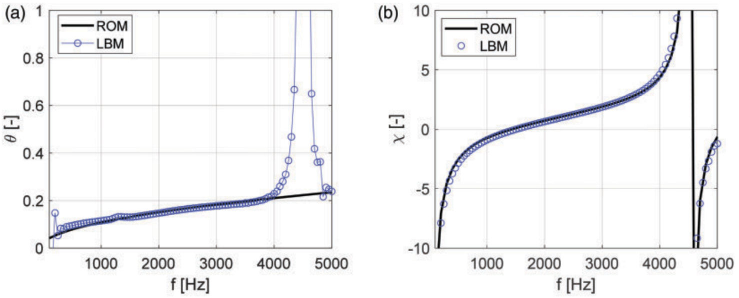

Figure 1.18: SDoF liner impedance predictions from high-fidelity LBM simulations in comparison to Goodrich linear impedance model. [42]

where $k_s = \sqrt{\omega\rho/\mu}$, c is the speed of sound, $k = \omega/c$ is the wavenumber, ρ is the fluid density, μ is the fluid viscosity and a is the perforate hole radius. The results overlap over a wide frequency range except for the anti-resonance frequency, this effect is not captured by the ROM but is of little significance. Therefore, the Goodrich Model can be considered accurate in this case (figure 1.18).

Non-linear Effects

In the case of high SPL, the contribution of non-linear effects becomes non-negligible, and it becomes necessary to also include the second term of the Goodrich model:

$$z_{nl} = \left[\frac{1.336541}{2c} \frac{(1-\sigma^2)}{\sigma^2 C_d^2} - i \left(2.07e-2[s] \frac{k}{\sigma^2} \right) \right] u_{rms} \tag{1.11}$$

with

$$u_{rms} = \sqrt{\sum \hat{u}^2} \tag{1.12}$$

and

$$|\hat{u}| = \frac{\left| p_{ref} 10^{\frac{SPL}{20}} \right|}{|z|\,\rho c} \tag{1.13}$$

where C_d is the discharge coefficient and have the empirical formulation:

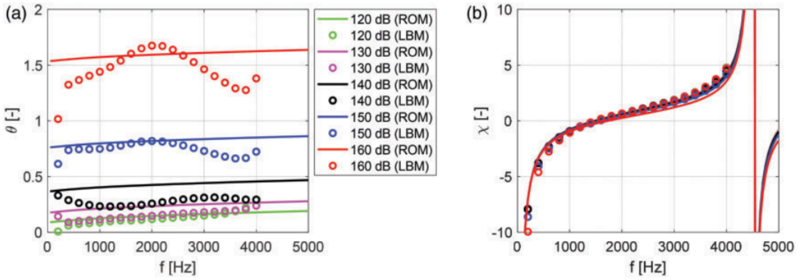

Figure 1.19: High SPL SDoF liner impedance predictions using high-fidelity LBM simulations with broadband source of different OASPL, in comparison to the ROM [42]

$$C_d = 0.80695\sqrt{\sigma^{0.1}e\frac{0.5072t}{d}} \tag{1.14}$$

In this case, the solution must be found iteratively, due to the dependence of z_{nl} from $\hat{u}$. Very good agreement is found between all methods for the reactance, but ROM predictions show a much more pronounced peak near resonance with the add of equation 1.11, the disagreement increases as the dB level increases entering the nonlinear regime, the level of agreement is nevertheless satisfactory (figure1.19).

Grazing Flow

To account for the grazing flow effect, the addition of a third term to the Goodrich Model is therefore necessary:

$$z_{gf} = \frac{1}{\sigma}\frac{1}{2+1.256\delta^*/d}M_{gf}+ \tag{1.15}$$

$$+i\left\{\frac{\omega t}{c\sigma}\left[1+\left(9+\frac{(k_s a)^2}{2}\right)^{-0.5}+2\frac{8a}{3\pi t}\frac{1-0.7\sqrt{\sigma}}{1+305M_{gf}^3}\right]-\cot(kh)\right\}$$

where $\delta*$ is the displacement thickness. A good level of agreement between the impedance values obtained with the Goodrich model and those calculated with LBM VLES using the Dean microphone method has been demonstrated (figure 1.20).

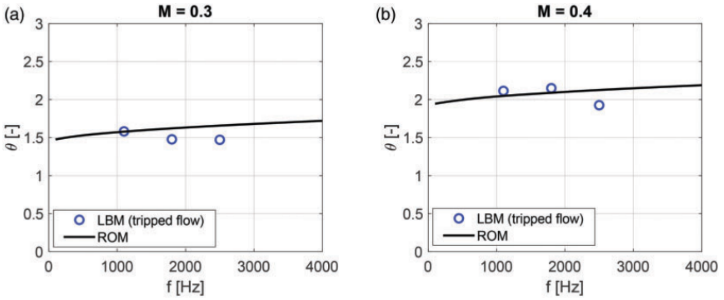

Figure 1.20: Grazing flow SDoF liner impedance predictions from high-fidelity LBM simulations for 130 dB excitation, compared to semi-empirical ROM. [42]

Bias Flow

To account for the bias flow effect, the addition of another term is necessary for Goodrich model:

$$z_{bf} = \frac{1}{\sigma}\frac{\pi ka}{2\left(\gamma^2+\delta^2\right)}(\delta + i\gamma) - i\cot(kD) \tag{1.16}$$

with

$$\gamma = \frac{I_1^2(\mathrm{St})\left(1+\frac{1}{\mathrm{St}}\right) + \frac{4}{\pi^2}\exp(2\mathrm{St})\cosh(\mathrm{St})K_1^2(\mathrm{St})\left(\cosh(\mathrm{St}) - \frac{\sinh(\mathrm{St})}{\mathrm{St}}\right)}{I_1^2(\mathrm{St}) + \frac{4}{\pi^2}\exp(2\mathrm{St})\cosh^2(\mathrm{St})K_1^2(\mathrm{St})} \tag{1.17}$$

and

$$\delta = \frac{\frac{2}{\pi \mathrm{St}} I_1(\mathrm{St})K_1(\mathrm{St})\exp(2\mathrm{St})}{I_1^2(\mathrm{St}) + \frac{4}{\pi^2}\exp(2\mathrm{St})\cosh^2(\mathrm{St})K_1^2(\mathrm{St})} \tag{1.18}$$

where I_1 and K_1 are the modified Bessel function and $S_t = ka/M_{bf}$ is the orifice Strouhal number.

1.2.2 Reformulation of Kooi's Equation

Murray et al [33] validated a low cost liner impedance model for SDoF liners. In situ measurements were performed in the Federal University of

Santa Catarina grazing flow duct facilities using Dean's in situ method that assume only plane wave and fully reflective walls, under both grazing flow and high SPL. Test were performed both in pure tone and broadband source. Semi-empirical impedance model adopted is a reformulation of the Kooi's equations with the addition of a nonlinear term. The normalized resistance:

$$\theta = \theta_{\text{lin,no flow}} + \theta_{\text{lin,grazing flow}} + \theta_{\text{non-lin}} \tag{1.19}$$

$$\theta_{\text{lin,no flow}} = \frac{k_1 \mu t}{\rho c \sigma C_D d^2} \tag{1.20}$$

$$\theta_{\text{lin, grazing flow}} = \frac{k_2 M \left[5 - \left(\frac{t}{d}\right)\right]}{4\sigma} - \frac{k_3 d f}{\sigma c} \tag{1.21}$$

$$\theta_{\text{non-lin}} = \frac{u' k_4 \left(1 - \sigma^2\right)}{2c \left(C_d \sigma\right)^2} \tag{1.22}$$

where the k_i are four constant and C_d is the discharge coefficient (setted to 0.76) and u' the acoustic velocity. For normalized reactance:

$$\chi = \chi_m + \chi_c \tag{1.23}$$

where the former is the facing sheet reactance, the latter is the cavity reactance:

$$\chi_m = k(t + \varepsilon d)/\sigma \tag{1.24}$$

with

$$\varepsilon = \frac{0.85(1 - 0.7\sigma^{0.5})}{(1 + 200M^3)} \tag{1.25}$$

and

$$\chi_c = -\cot(kh) \tag{1.26}$$

where ε represents a corrective term. The semi-empirical impedance model provides a good confidence in the evaluation of resistance and reactance (figure: 1.21)

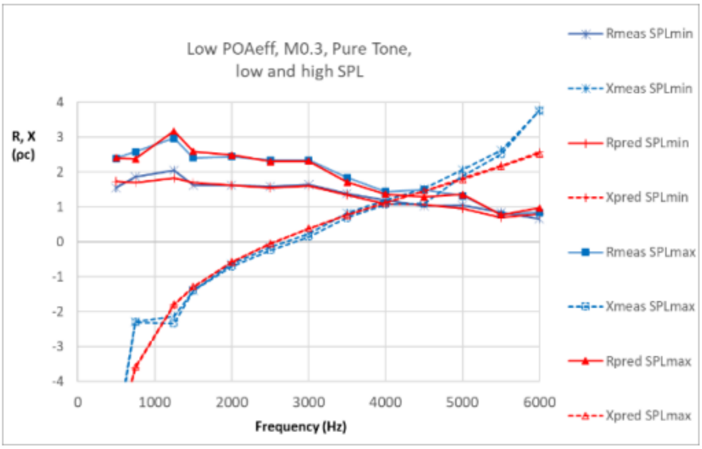

Figure 1.21: SDoF Perforate Impedance Prediction vs Measurement, low POA, varying SPL. [33]

1.2.3 Hersh Model

Giaccherini et al [20] validated a model for the acoustic impedance of triple degree of freedom (TDOF) liner, extension of the analytical model provided by Hersh for SDoF and DDoF liners. The Hersh model is based on the assumption that the liner functions as a Helmholtz resonator, this is true when the wavelength of the acoustic wave is much greater than the size of the cell. The original Hersh model for the evaluation of SDoF liners impedance shows excellent agreement with high fidelity result and in case of low SPL and very low grazing flow speed, the following models for linear resistance and reactance are obtained:

$$\frac{X}{\rho_0 c_0} = \frac{\omega H_1}{\sigma_1 c_0} - \cot kL_1 \tag{1.27}$$

$$\frac{R_L}{\rho_0 c_0} = (\frac{4\nu_0 w_1}{\sigma_1 c_0 d_1^2})\left[K_{SS} + K_{ac}\sqrt{\frac{\omega d_1^2}{\nu_0}}\right] \tag{1.28}$$

In the presence of high SPL and grazing flow, the formulation for resistance can be extended as follows:

$$\frac{R}{\rho_0 c_0} = \sqrt{(\frac{1-C_d}{C_d})(\frac{P_0}{\rho_0 c_0^2 \sigma_1^2}) + (\frac{VC_V}{2\sigma_1 c_0} + \frac{R_L}{2\rho_0 c_0})^2} + (\frac{R_L}{2\rho_0 c_0}) \tag{1.29}$$

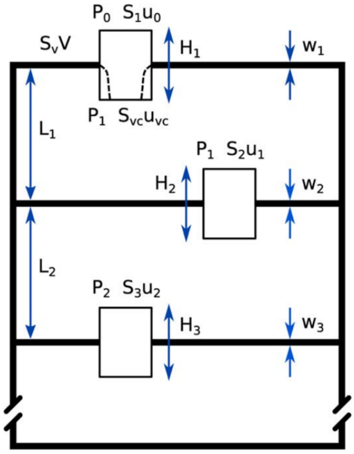

Figure 1.22: Control volumes for the Hersh model derivation. [20]

where: P_0 is the amplitude of the acoustic pressure at the neck ends, w_1 the facesheet thickness, H_1 is the inertial length of the air mass oscillations, K_{SS} and K_{ac} are empirical constant function of d_1/w_1, S_1 is the orifice cross-sectional area, S_{vc} is the vena contracta area due to blockage effects, S_V the grazing flow cross sectional area, $C_d = S_{vc}/S_1$ the acoustic discharge coefficient and $C_V = S_V/S_1$ the grazing flow discharge coefficient.

If non-linear effects becomes non-negligible a frequency-dependent C_d is required to correctly reproduce the acoustic resistance over the entire frequency range. However, moving away from the linear regime with increasing SPL, the Hersh model becomes increasingly inaccurate. The effects of the SPL and the grazing speed can be embedded also into the reactance model, for this purpose, experimental campaigns are required to determine how the H_1 inertial length parameter is influenced by the high grazing speeds and the nonlinear SPL.

TDOF liner can be interpreted as a series of three independent Helmholtz Resonators with different cavity depth, facesheet thickness and orifice diameter, on the base of this interpretation, the Hersh model can easily be expanded to a case for TDOF liner. TDOF Hersh model extension proves reliable only for very high or very low frequencies. The difference between SDoF and TDOF liner is that the former generally has a single impedance minimum, while the latter has three valleys and two peaks of anti-resonance,

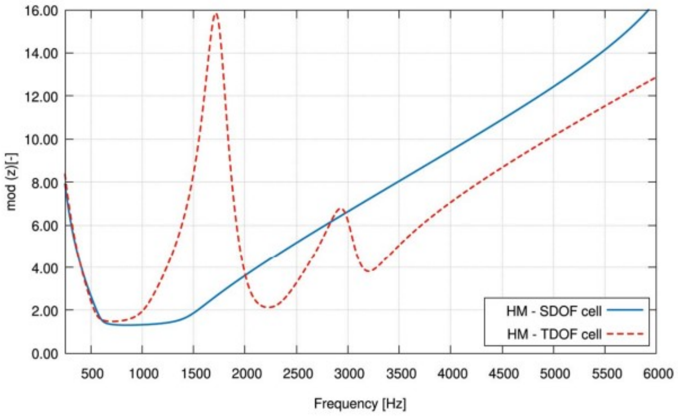

Figure 1.23: SDoF and TDOF impedance predicted by the Hersh model. [19]

for which there is no attenuation, the acoustic liner becomes transparent (figure 1.23). More minima ensure attenuation over a broader frequency range.

1.2.4 Motsinger and Kraft Model

Motsinger and Kraft [32] proposed an impedance model for SDoF liners that can be easily extended to the case of DDoF liners. The general nondimensional impedance formula for a SDoF liner is [10]:

$$z = \theta + i(\chi_m + \chi_c) \tag{1.30}$$

where θ is the porous-surface resistance, χ_m is the porous-surface mass reactance and χ_c is the cavity reactance:

$$\chi_c = -\cot(kh) \tag{1.31}$$

where h is the total honeycomb thickness (figure 1.24). For a DDoF liner, the general formula becomes:

$$z = z_1 + \left[\frac{\left(z_2 \dfrac{\cos(kh_1)\sin(kh_2)}{\sin(kh)} - i\cot(kh) \right)}{1 + iz_2 \dfrac{\sin(kh_1)\sin(kh_2)}{\sin(kh)}} \right] \tag{1.32}$$

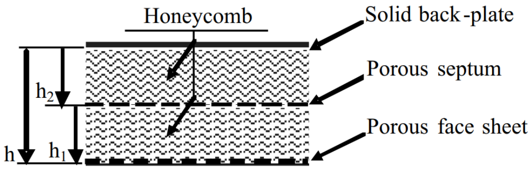

Figure 1.24: Illustration of DDoF liners. [10]

where:

$$z_1 = \theta_1 + i\chi_1 \tag{1.33}$$

$$z_2 = \theta_2 + i\chi_2 \tag{1.34}$$

Supposing that acoustic levels are not high enough to induce nonlinear energy losses, only linear contributions are considered:

$$\theta = \theta_{lin,noflow} + \theta_{lin,grazingflow} = \frac{64\mu\tau}{2\rho c\sigma C_d d^2} + \frac{M_e}{\sigma\left(2 + 1.256\frac{\delta*}{d}\right)} \tag{1.35}$$

$$\chi_m = \frac{k[\tau + 0.85d(1 - 0.7\sqrt{\sigma})/(1 + 305M_e^3)]}{\sigma} \tag{1.36}$$

where τ is the porous-surface thickness, M_e is the boundary-layer asymptotic Mach number, $\delta*$ is the boundary-layer displacement thickness, $\sigma = N_s\pi d^2/4$ is the surface porosity defined as the ratio between the orifices area and the total area, N_s being the number of orifices for unit surface.

1.3 Optimization

Winkler et al [42] showcase a liner design approach considered representative for the aerospace industry (figure 1.27). The liner design approach is divided into 3 steps, the first involves impedance optimization, the second evaluates the attenuation in the far field, and finally, the calculation of the Effective Perceived Noise Level (EPNL) based on flight trajectories. The optimization cycle aims to define the liner specifications that best match the target, based on a defined target attenuation spectrum. In fact, some geometric parameters of the liners, such as the POA σ, the width d and

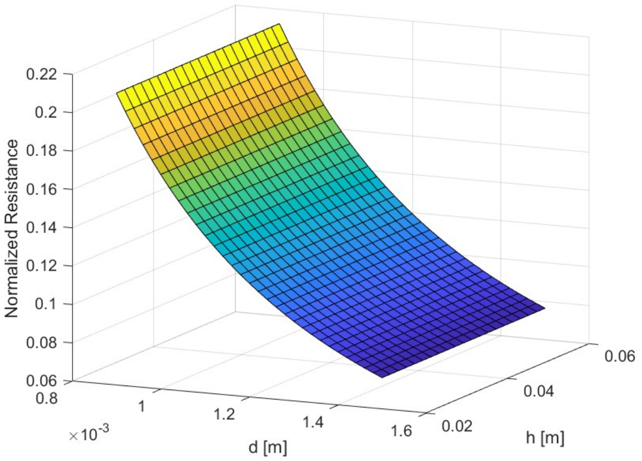

Figure 1.25: Normalized Resistance Motsinger and Kraft Model (SDoF)

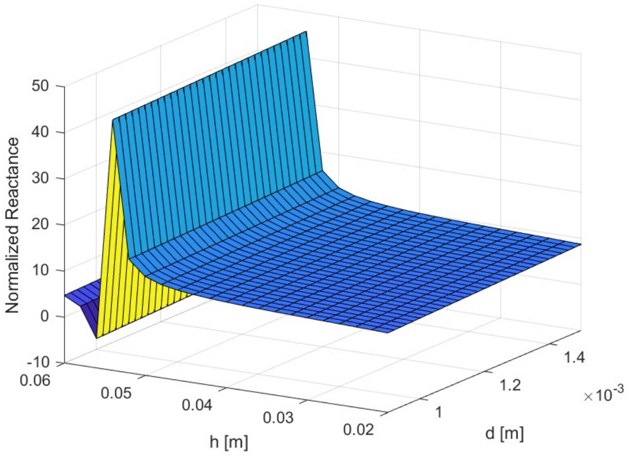

Figure 1.26: Normalized Reactance Motsinger and Kraft Model (SDoF)

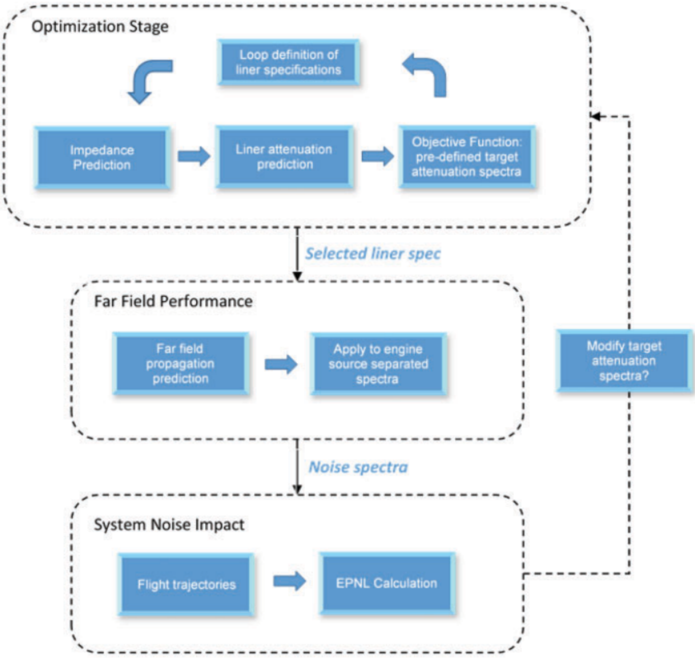

Figure 1.27: Summary of the liner design process. [42]

depth h of each core cavity, along with their number [15], can be optimized to maximize their performance in terms of directivity or acoustic emission intensity, allowing compliance with regulations. In addition to a reliable model for acoustic impedance prediction, a finite element acoustic prediction software like Actran is incorporated into the optimization process, enabling the evaluation of acoustic emissions in far field based on input data such as noise excitation, boundary conditions and CFD field previously solved.
Dilillo et al [14] investigated the effect of the engine fan source (instead of using the easier assumption of equal energy per propagation mode source) and the wall boundary layer refraction (instead of using the easier assumption of uniform flow), the impedance was first optimized while neglecting theirs effects, and then re-optimized taking them into account. Optimization is carried out for three liner designs (linear SDoF, perforated SDoF and DDoF) by minimizing the SPL at a distance of 18.5 meters from the duct, for angles between 40° and 90°, with an Engine Order (EO) ranging from 6 to 83 and using NextGen Liner Multiphysics Code (NLMC). NLMC is a propagation code written in MATLAB that propagates the fan source modes

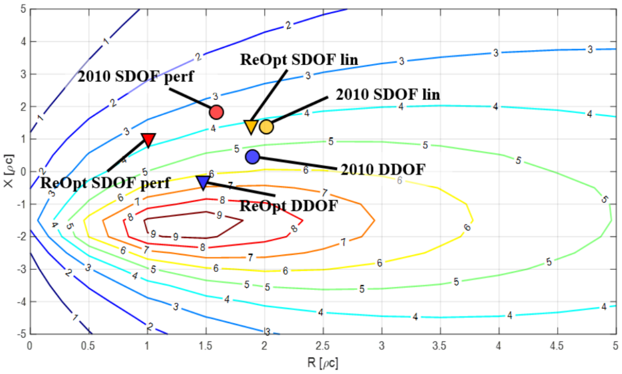

Figure 1.28: Predicted levels of the overall attenuation in the far-field for optimised and re-optimised design. [14]

along a cylindrical inlet duct in presence of shear flow predicting directivity and EPNL for a given flight path. This code ensures very fast computational evaluations (order of second for each cut-on mode), allowing it to be coupled with the Matlab Optimization Toolbox in order to obtain impedance that minimise cost function. However, the reduced computation time is due to the following assumptions: rigid and fully-lined cylindrical duct, adiabatic and inviscid flow, constant thickness boundary layer and uniform impedance modeled using Leonardo semi-empirical model. The results showed that not including the effects of the engine fan source and the boundary layer in the optimization process leads to an inaccurate prediction of liner performance, with an overestimation of liner attenuation. Furthermore, the geometry has a significant impact: DDoF liners and linear SDoF liner are more sensitive than perforate SDoF liner. The optimal impedance of perforated SDoF liners varies much less when re-optimized considering the boundary layer and engine fan source (figure 1.28). It is therefore concluded that it is important to include both effects in liner design.

In a later work [15], the NLMC was used by Dilillo et al to optimise liner geometry minimising various objective functions on a desired frequency bandwidth considering both the impact of the engine fan noise modal content and that of the wall boundary layer on the design of the inlet liner. Impedance was modeled using weighted admittance approach [25]. The optimization was performed for two different liners, one with a total panel depth of 24mm and another one deeper at 40mm, each of them optimized for a four-cavity cluster and a six-cavity cluster case. In a first case, the

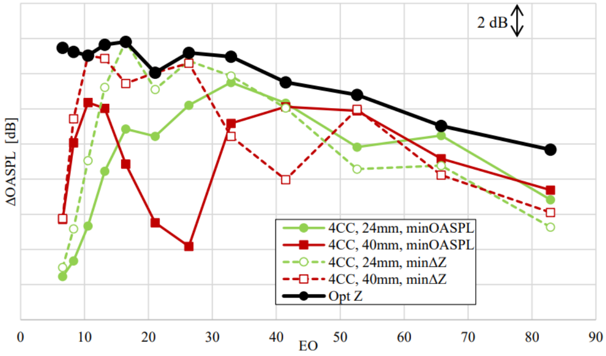

Figure 1.29: Predicted attenuation of the hard wall overall SPL in the far-field, at 18.5m from the duct end, between 40° and 90°, for a subset of four-cavity cluster-based ComplexCav geometries. [15]

choice was to minimize the Overall Sound Pressure Level (OASPL), and in a second case, it was to minimize the ΔZ (minimising the difference with the optimum impedance in the $6 < EO < 83$ interval evaluated in the previous work). The results show that significantly greater attenuation (where $\Delta OASPL = OASPL^{HardWall} - OASPL^{lined}$) can be achieved by minimizing the OASPL, especially in the case of a 24mm depth with a four-cavity cluster and in the case of a 40mm deep cavity with a six-cavity cluster (figure 1.29). Results for optimised liners are also compared to the performance of traditional liners (figure 1.30), highlighting a higher attenuation at higher EO for both $6CC, 40mm, minOASPL$ and $4CC, 24mm, minOASPL$ and lower EO for $6CC, 40mm, minOASPL$.

1.4 Objectives

This thesis aims at defining the geometric parameters of a liner that minimizes the SPL in the far-field and ensures an optimum in term of directivity. To do this, the aeroacoustic simulation code Actran is used, providing a normalized impedance value as a boundary condition, obtained by modifying parameters within a previously selected model. Once the simulation setup is validated, it will be possible to proceed with initial parametric evaluations, assessing how the variation of a specific geometric parameter and different flow conditions affect the SPL values detected by the microphones in the

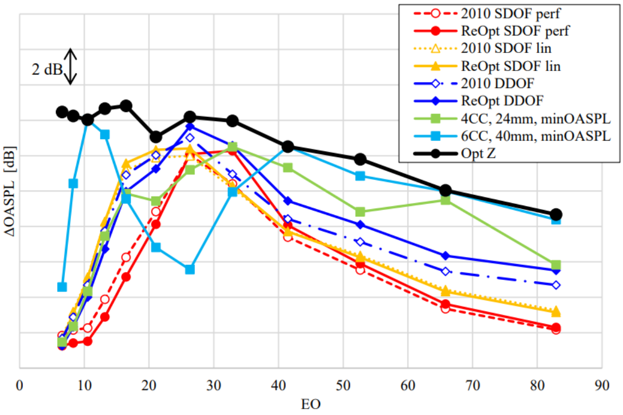

Figure 1.30: Predicted attenuation of the hard wall overall SPL in the far-field at 18.5m from the duct end, between 40° and 90°, using the measured fan noise source and assuming shear flow in the inlet duct. [15]

far field. Finally, the intention is to automate the process by coupling the NLopt optimization library with Actran to evaluate the optimal point corresponding to the minimum of a specific objective function. In doing so, one also aims to evaluate the effect that different optimization approaches and various choices regarding optimization parameters have on the search for the minimum.

Chapter 2

Actran DGM

Actran is a simulation software developed by Free Field Technologies (FFT) for modelling sound propagation, transmission and absorption in an acoustic, vibro-acoustic or aero-acoustic context. Particularly, Actran DGM module implements the discontinuous Galerkin method for solving the Linearized Euler Equations. It is designed for predicting the propagation of tonal engine noise components in a moving fluid with shear layers and in the presence of acoustically lined ducts, as typically happens in engine nacelle exhausts [1].

2.1 General Description of the process

Actran DGM employs an hybrid method that distinctly separates the computation of the fluid dynamics solution from the acoustic one, unlike direct methods where the two fields are directly solved together. This separation is driven by the difficulty of solving both fields together, given the significant disparity in terms of energy content and the difference between the size of turbulent structures and the wavelength of acoustic propagation [18]. This allows for a significant reduction in computational cost. The assumption underlying these methods is that the effect of the acoustic field on the fluid dynamics field is negligible, thus allowing the flow to generate acoustic waves that do not exhibit a retroactive effect on the flow [18]. The process generally involves four steps (figure 2.1) [1]:

- **Computational Fluid Dynamics Analysis:** the fluid dynamics field is evaluated outside of Actran using one of the compatible computa-

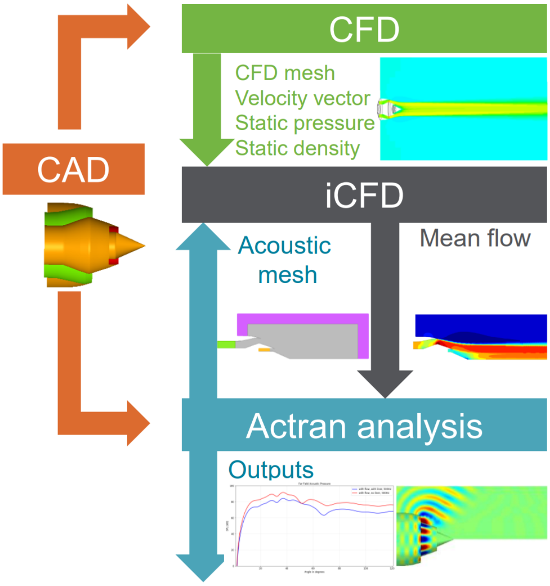

Figure 2.1: Computational process of a complete ACTRAN DGM analysis. [4]

tional fluid dynamics software such as Star CCM+, OpenFOAM, and ANSYS Fluent.

- **Integrated Computational Fluid Dynamics Analysis:** the fluid dynamics field previously evaluated on the fluid dynamics mesh is re-interpolated onto the acoustic mesh in Actran. This allows for the calculation of source terms that will appear on the right-hand side of the Euler equations.

- **Acoustic Analysis:** the fluid dynamics field (i.e. u_0, p_0, ρ_0 distributions) and the previously evaluated source terms are taken as input to solve the linearized Euler equations

- **Post processing:** the solution in the far field is evaluated through the FWH analogy.

2.2 Near Field analysis

Actran DGM solves the Linearized Euler Equations (LEE) in time domain through an iterative approach until achieving an harmonic steady-state solution (convergence is checked on the surface between the buffer region and the radiation domain) [1]. Since the phenomenon of acoustic propagation is isoentropic, it can be studied starting from the Euler equations [5]:

$$\begin{cases} \frac{\partial \rho}{\partial t} + \rho \nabla \cdot \mathbf{u} + \mathbf{u} \cdot \nabla \rho = 0 \\ \rho \left(\frac{\partial \mathbf{u}}{\partial t} + \mathbf{u} \cdot \nabla \mathbf{u} \right) = -\nabla p \\ \rho T \left(\frac{\partial s}{\partial t} + \mathbf{u} \cdot \nabla s \right) = 0 \end{cases} \tag{2.1}$$

By separating the quantities of the propagation medium from those of the acoustic perturbation, which we know to be small compared to the former, it is possible to perform a linearization:

$$\begin{aligned} \mathbf{u} &= \mathbf{u}_0 + \mathbf{u}', \qquad && \left| \frac{\mathbf{u}'}{\mathbf{u}_0} \right| \ll 1, \\ p &= p_0 + p', && \frac{p'}{p_0} \ll 1, \\ \rho &= \rho_0 + \rho', && \frac{\rho'}{\rho_0} \ll 1, \\ c &= c_0 + c', && \frac{c'}{c_0} \ll 1. \end{aligned}$$

$$\frac{\partial \rho'}{\partial t} + (\rho_0 + \rho') \nabla \cdot (\mathbf{u_0} + \mathbf{u}') + (\mathbf{u_0} + \mathbf{u}') \cdot \nabla (\rho_0 + \rho') = 0 \tag{2.2}$$

and collecting the terms of order 1 and those of the acoustic oscillation order:

$$\nabla \cdot (\rho_0 \mathbf{u_0}) = 0 \tag{2.3}$$

$$\frac{\partial \rho'}{\partial t} + \rho_0 \nabla \cdot \mathbf{u}' + \rho' \nabla \mathbf{u_0} + \mathbf{u_0} \cdot \nabla \rho' + \mathbf{u}' \cdot \nabla \rho_0 = 0 \tag{2.4}$$

By applying the same procedure to the momentum and energy balance equations the linearized Euler equations are obtained:

$$\begin{cases} \frac{\partial \rho'}{\partial t} + \mathbf{u}_0 \cdot \nabla \rho' + \mathbf{u}' \cdot \nabla \rho_0 + \rho_0 \nabla \cdot \mathbf{u}' + \rho' \nabla \cdot \mathbf{u}_0 = 0, \\ \rho_0 \left(\frac{\partial \mathbf{u}'}{\partial t} + \mathbf{u}_0 \cdot \nabla \mathbf{u}' + \mathbf{u}' \cdot \nabla \mathbf{u}_0 \right) + \rho' \mathbf{u}_0 \cdot \nabla \mathbf{u}_0 = -\nabla p', \\ \rho_0 T_0 \left(\frac{\partial s'}{\partial t} + \mathbf{u}_0 \cdot \nabla s' + \mathbf{u}' \cdot \nabla s_0 \right) + (\rho_0 T' + \rho' T_0)\, \mathbf{u}_0 \cdot \nabla s_0 = 0, \end{cases} \tag{2.5}$$

The resolution of these equations allows for the assessment of the propagation of small acoustic perturbations within a given mean flow. Depending on the cases, Actran allows choosing whether to solve the Isentropic Linearized Euler Equations or the Homentropic Linearized Euler Equations. The former is composed of a set of 5 differential equations (in 3D case) and describes a more general case, thus ensuring a broader range of validity as it is applicable for the propagation of acoustic fluctuations in rotational mean flows, in supersonic mean flows, and through a shock. This solution, however, has the disadvantage of requiring the solution of one additional equation compared to the homentropic system, in which some physical aspects of acoustic propagation are not accurately modeled [2]. This is due to the fact that in a homoentropic process, entropy remains constant in space and time. As a result, the conservation equation of acoustic energy is automatically satisfied, reducing the dimension of the system of equations to be solved. However, this simplification leads to an inaccurate description of acoustic energy transport under certain conditions, such as in the presence of shocks, where there is an entropy jump.

Homoentropic Linearized Eulerian Equation

In an homoentropic process $\frac{\partial s'}{\partial t} = \nabla s' = 0$. [2]

$$\begin{cases} \frac{\partial \rho'}{\partial t} + \nabla \cdot (\rho_0 \mathbf{u}' + \rho' \mathbf{u_0}) = 0 \\ \rho' \mathbf{u_0} \cdot \nabla \mathbf{u_0} + \rho_0 (\frac{\partial \mathbf{u}'}{\partial t} + \mathbf{u}' \cdot \nabla \mathbf{u_0} + \mathbf{u_0} \cdot \nabla \mathbf{u}') = -\nabla (c^2 \rho') \end{cases} \tag{2.6}$$

Energy equation is automatically satisfied.

Isentropic Linearized Eulerian Equation

In an isentropic process $\frac{\partial s'}{\partial t} + \mathbf{u_0} \cdot \nabla s' = 0$ [2].

$$\begin{cases} \frac{\partial \rho'}{\partial t} + \nabla \cdot (\rho_0 \mathbf{u}' + \rho' \mathbf{u_0}) = 0 \\ \rho' \mathbf{u_0} \cdot \nabla \mathbf{u_0} + \rho_0 (\frac{\partial \mathbf{u}'}{\partial t} + \mathbf{u}' \cdot \nabla \mathbf{u_0} + \mathbf{u_0} \cdot \nabla \mathbf{u}') = -\nabla p' \\ \frac{\partial p'}{\partial t} + \mathbf{u_0} \cdot \nabla p' + \mathbf{u} \cdot \nabla p_0 = c^2 (\frac{\partial p'}{\partial t} + \mathbf{u_0} \cdot \nabla \rho' + \mathbf{u} \nabla \rho_0) \end{cases} \tag{2.7}$$

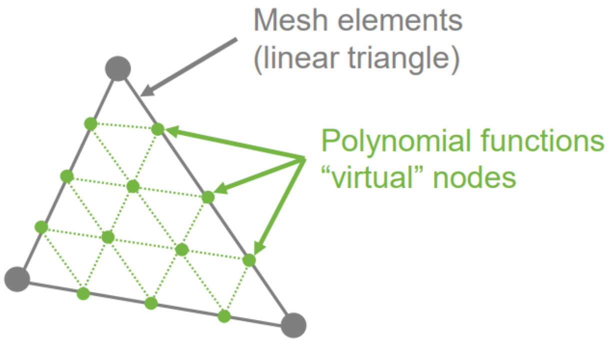

Figure 2.2: Example: 4th order element [2]

2.2.1 Mesh and Solution Scheme

The Discontinuous Galerkin method used for solving Linearized Euler Equations combines the high parallelizability of a finite volume scheme with the accuracy of a finite element method [1]. One characteristic of the Discontinuous Galerkin method is that degrees of freedom are not shared between neighboring elements. This implies that the solution could be different on the two sides of an element face, and continuity is not enforced. Therefore, the discontinuity becomes a measure of solution convergence.
The acoustic domain is meshed using triangular elements in 2D and axisymmetric configurations (figure 2.2) and the numerical quality of the simulation is measured by:

- **Dispersion error:** related to the change in propagation speed with respect to the expected one.
- **Dissipation error:** related to amplitude decrease along the acoustic propagation path.

Each element order is automatically adapted from 1 to 16 to minimize these errors and maintaining the same level of accuracy across the entire domain based on the local minimal wavelength [3]:

$$\lambda_{min} = \frac{c - ||\mathbf{u_0}||}{f} \tag{2.8}$$

In particular:

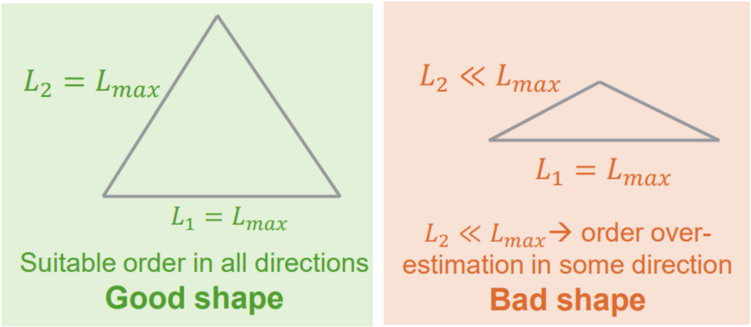

Figure 2.3: Example of Good and Bad shape for mesh elements. [3]

- if the elements are large (high L_{max} and small $\frac{\lambda_{min}}{L_{max}}$) the order of the element increases to accurately represent the small length scales
- if the elements are small (small L_{max} and large $\frac{\lambda_{min}}{L_{max}}$) low order can be used as spatial fluctuation are larger relatively to the element size.

For efficiency reason mesh generation should target an order of 6, this order is achieved by constructing the mesh in such a way that:

$$\lambda_{min} < L_{max} < 1.5\lambda_{min}$$

It is also important that the elements are as equilateral as possible for faster computation because highly distorted elements can cause an overestimation of the order for the side with a smaller dimension than L_{max}, resulting in a decrease in efficiency (figure 2.3). Very small elements are still necessary in some situations to properly discretize geometries or the flows.
Assuming the following as the general form of the equations [1]:

$$\frac{\partial \mathbf{q}}{\partial t} + \nabla \cdot (\mathbf{F} \cdot \mathbf{q}) = \mathbf{s} \cdot \mathbf{q} \tag{2.9}$$

(where the values of F_j contains local mean flow information and q is a vector where all unknowns are store), the spatial discretization of the problem can be carried out as follows:

$$\int_\Omega \mathbf{N}_\alpha \frac{\partial \mathbf{q}}{\partial t} dV = \int_\Omega \nabla \cdot (\mathbf{N}_\alpha \mathbf{F} \cdot \mathbf{q}) + \mathbf{N}_\alpha \mathbf{s} \cdot \mathbf{q} dV - \oint_{\partial\Omega} \mathbf{N}_\alpha \mathbf{F} \cdot \mathbf{q} \cdot \mathbf{n} dS \tag{2.10}$$

where N_α is the *Lagrange polynomial function* (order from 1 to 16) for interpolation on mesh element, dS is the the surface delimiting one element and dV is the volume of one element.
Regarding the temporal discretization, Actran DGM utilizes the Runge-Kutta scheme for its properties in terms of accuracy and stability, by default a 4th order Runge Kutta scheme is use. This time scheme is explicit and the time step is therefore limited by a Courant-Friedrichs-Lewy (CFL) like condition. The CFL condition is a numerical stability criterion used to determine the time step in a numerical scheme. This condition is particularly important in explicit time schemes because it directly affects the stability of the numerical solution. More specifically, it requires that the time step be smaller than a critical value to ensure the correct propagation of information through the grid. For the specific case of Actran:

$$\Delta(t) \leq C(p)\frac{r}{v+c} \tag{2.11}$$

where:

- $C(p)$: $\dfrac{1}{2p+1} \Rightarrow$ CFL number
- p: element order
- r: radius of the element inscribed sphere
- c: speed of sound
- v: mean flow velocity norm

From this, it follows that, since the timestep of the global simulation is the smallest timestep among all elements, elements that are too small have to be avoided to reduce the computation time, therefore, a single skewed element can impact the performance of the whole model, hence, in this case as well, the mesh should have elements as equilateral as possible (figure 2.4). An appropriate CFL parameter helps avoid numerical instability issues. The CFL condition can also be interpreted as the requirement that the distance traveled by a wave during one timestep must be less than the length of the element (figure 2.5) [3].

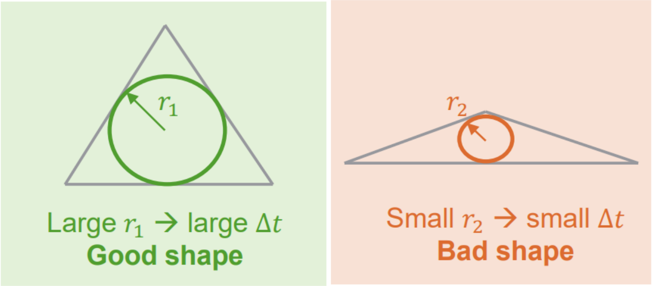

Figure 2.4: Example of Good and Bad shape for mesh elements[3]

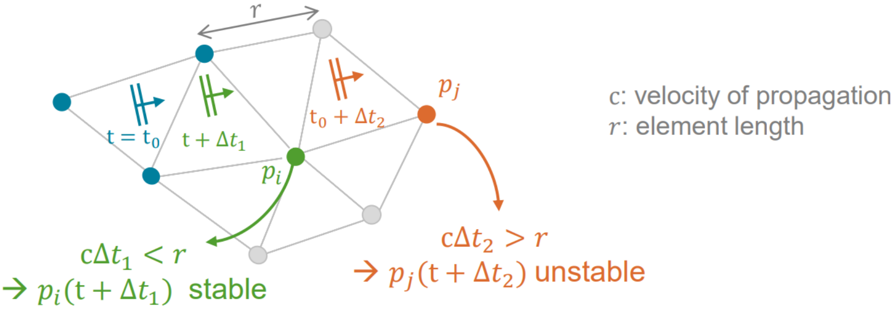

Figure 2.5: How to interpret the CFL criterion [3]

2.2.2 Boundary Conditions

Non-reflecting boundary condition

To allow propagation in free field, this condition enforces that all the incoming modes are set to zero while allowing outgoing modes to propagate outside [1]. This condition is easy to enforce if the waves propagate perpendicularly to the wall; however, it becomes more complex when the propagation is transverse. This can result in potential reflection in the presence of transverse components. Since this surface is located close to the near field to reduce computational costs, such spurious numerical reflection can influence the solution. To minimize this effect, the non-reflecting surface is preceded by a buffer zone that intervenes by gently damping the outgoing waves.

Buffer Zones

In this zone (figure 2.6), damping is added to the numerical scheme progressively along the thickness of the Buffer Zone as follows [1]:

$$\sigma(x) = \sigma_{max}|1 + \frac{d(x) - L}{L}|^{\beta} \tag{2.12}$$

where σ_{max} is the value of the damping near the non-reflecting boundary condition, L is the thickness of the buffer zone, β controls the order of the damping increase and d(x) is the distance from the point considered to the bottom of the buffer zone.

Wall condition

The wall condition imposes that the normal velocity component u_n is set to zero. This condition generates a pure reflection of the acoustic waves [1].

Admittance

Admittance is the inverse of impedance. This boundary condition allows us to simulate the presence of acoustic treatment in the simulation. In the frequency domain, this condition is expressed in frequency domain as [1]:

$$u'_n = A(\omega)p' \tag{2.13}$$

where $A(\omega)$ is the admittance value.

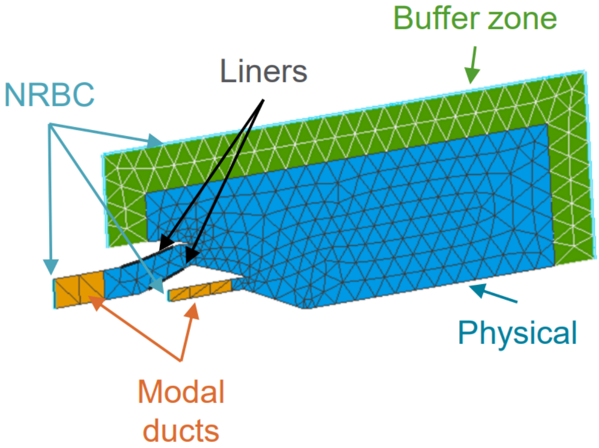

Figure 2.6: Acoustic analysis domain components [4]

2.2.3 Aeroacoustic Sources

Actran DGM allows for the calculation of aeroacoustic sources, introduced as additional terms on the right-hand side of the Linearized Euler Equations that in non conservative form and in the presence of source terms can be expressed as follows [1]:

$$\begin{cases} \dfrac{\partial \rho'}{\partial t} + \nabla \cdot (\rho' \mathbf{u_0} + \rho_0 \mathbf{u}') = Q_p \\ \rho' \mathbf{u_0} \cdot \nabla \mathbf{u_0} + \rho_0 (\dfrac{\partial \mathbf{u}'}{\partial t} + \mathbf{u}' \cdot \nabla \mathbf{u_0} + \mathbf{u_0} \cdot \nabla \mathbf{u}') + \nabla p = Q_m \\ (\dfrac{D\rho'}{Dt} + \mathbf{u}' \cdot \nabla \rho_0) c_0^2 = Q_s \end{cases} \tag{2.14}$$

where Q_p is the mass source, Q_m is the momentum source and Q_s is the energy source. This calculation is performed based on a CFD file provided as input, originating from one of the compatible computational fluid dynamics simulation software like Star CCM+, Ansys Fluent, or OpenFOAM, this procedure allows for the calculation of p_0, ρ_0, $\mathbf{u_0}$ which must be known to proceed with the resolution of the LEE. Depending on the theory used these terms can take different forms, in fact Actran DGM implements various aeroacoustic models. The aeroacoustics models are presented below with the indicial notation as it appears in the original papers [9], [31] and [41] in which they were introduced, which is preferred for a simplification of the treatment, where:

- $\dfrac{\partial(u_j)}{\partial x_j} = \nabla \cdot (\mathbf{u})$
- $\dfrac{\partial(\rho u_j)'}{\partial x_j} = \nabla \cdot (\rho' \mathbf{u_0} + \rho_0 \mathbf{u}')$

Bogey, Bailly & Juvé model

The source terms are computed from a CFD solution obtained by solving the unsteady Navier-Stokes equations with an appropriate turbulence model. Bogey et al. proposed as follows [9]:

$$\begin{cases} \dfrac{\partial \rho'}{\partial t} + \dfrac{\partial(\rho u_j)'}{\partial x_j} = 0 \\ \dfrac{\partial(\rho u_i)'}{\partial t} + \dfrac{\partial[\bar{u}_j(\rho u_i)' + \bar{u}_i(\rho u_i)' - \rho'\bar{u}_i\bar{u}_j + p'\delta_{ij}]}{\partial x_j} = -\dfrac{\partial(\mathbf{T_{ij}})}{\partial x_j} \\ \dfrac{\partial(\rho e)'}{\partial t} + \dfrac{\partial[\bar{h}(\rho u_j)' + \bar{u}_j(\rho h)' - \rho'\bar{h}\bar{u}_j]}{\partial x_j} = 0 \end{cases} \tag{2.15}$$

$$\delta_{ij} \equiv \begin{cases} 0 & \text{for } i \neq j \\ 1 & \text{for } i = j. \end{cases}$$

where $\mathbf{T_{ij}} = \rho u_i' u_j' - \overline{\rho u_i u_j}$, e and h denotes the energy and enthalpy respectively. The over bar terms denote time averaging resulting from Reynolds decomposition.

Turbulent Entropic model

Billson et al. proposed the Turbulent Entropic model [31]. Unlike the previous one, in this model, there are two source terms. The first is the derivative of the Reynolds stress tensor appearing in the momentum equation, and the second is a function of temperature appearing in the energy balance equation [1]:

$$\begin{cases} \dfrac{\partial \rho'}{\partial t} + \dfrac{\partial(\rho u_j)'}{\partial x_j} = 0 \\ \dfrac{\partial(\rho u_i)'}{\partial t} + \dfrac{\partial[\bar{u}_j(\rho u_i)' + \bar{u}_i(\rho u_i)' - \rho'\bar{u}_i\bar{u}_j + p'\delta_{ij}]}{\partial x_j} = -\dfrac{\partial(\mathbf{T_{ij}})}{\partial x_j} \\ \dfrac{\partial(\rho e)'}{\partial t} + \dfrac{\partial[\bar{h}(\rho u_j)' + \bar{u}_j(\rho h)' - \rho'\bar{h}\bar{u}_j]}{\partial x_j} = \dfrac{\partial(\mathbf{Q_i})}{\partial x_i} \end{cases} \tag{2.16}$$

where $\mathbf{T_{ij}} = \rho u'_i u'_j - \overline{\rho u_i u_j}$, $\mathbf{Q_i} = c_p(\rho T'' u''_i - \overline{\rho T u_i}) - \tilde{u}_j \mathbf{T_{ij}}$ and c_p is the heat capacity at constant pressure. Tilde variables and double prime represent the mean flow and fluctuating parts respectively using Favre's decomposition, that is an alternative way of decomposing a variable in time average plus a fluctuating part: $H(\mathbf{x},t) = \tilde{H}(\mathbf{x},t) + H''(\mathbf{x},t)$. To simplify the calculation, Actran DGM implements standard Reynolds's decomposition $H_0(\mathbf{x}) = \lim\limits_{T\to\infty} \frac{1}{T} \int_t^{t+T} H(\mathbf{x},t)$ instead of Favre's one.

Stochastic Noise Generated Randomly (SNGR) model

$$\begin{cases} \dfrac{\partial \rho'}{\partial t} + \dfrac{\partial (\rho u_j)'}{\partial x_j} = 0 \\ \dfrac{\partial (\rho u_i)'}{\partial t} + \dfrac{\partial [\bar{u}_j (\rho u_i)' + \bar{u}_i (\rho u_i)' - \rho' \bar{u}_i \bar{u}_j + p' \delta_{ij}]}{\partial x_j} = -\dfrac{\partial (\mathbf{T_{ij}})}{\partial x_j} \\ \dfrac{\partial (\rho e)'}{\partial t} + \dfrac{\partial [\bar{h} (\rho u_j)' + \bar{u}_j (\rho h)' - \rho' \bar{h} \bar{u}_j]}{\partial x_j} = 0 \end{cases} \tag{2.17}$$

where $\mathbf{T_{ij}} = \rho u^*_i u^*_j$. In the SNGR model [41], the source term is computed from synthesized turbulent velocities u^*_i generated as a sum of random Fourier modes and through a steady RANS-CFD solution for the calculation of the Turbulent Kinetic Energy, while in Bogey, Bailly & Juvé's model the velocities (and the other flow variables) are computed using a unsteady CFD method [1]. This approach allows for a reduction in the cost of CFD simulation. The basic assumptions are that the flow is incompressible and at a low Mach number, the reconstructed turbulence is homogeneous and isotropic, acoustic sources are spatially uncorrelated, and the velocity spectrum depends on local turbulent kinetic energy (TKE) [18].

2.3 Duct Modes

The methods described above are not accurate in assessing the noise generated by the fan due to the complex flow field through and downstream of it. Since this is the main cause of noise, it is crucial to have the most accurate representation, therefore, an injection of the modal content generated by the fan, previously evaluated through experimental [38] or numerical [11] methods, is introduced into the duct [1].

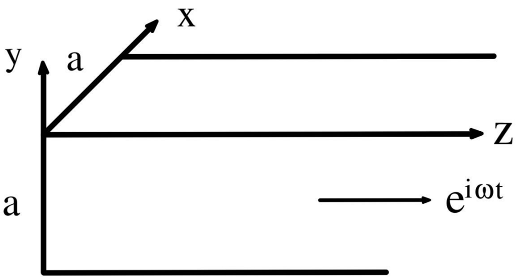

Figure 2.7: Rectangular Duct

2.3.1 Wave propagation in duct

In the context of wave propagation in a duct, only waveforms that satisfy the wave equation and the boundary conditions imposed by the walls, which are assumed to be non-absorbing and therefore rigid, exist. In this case, the solution of the wave equation can be represented as an expansion in a series of particular solutions called modes that satisfy the boundary conditions. For simplicity of treatment, a case with a rectangular duct and constant cross-section is presented (figure 2.7).

Through a linear combination of the Linearized Euler Equations, it is possible to obtain the wave equation for describing the propagation of acoustic waves in the medium [5]:

$$\frac{1}{c_0^2}\frac{\partial^2 p'}{\partial t^2} - \nabla^2 p' = 0 \tag{2.18}$$

Along the rigid walls, the following boundary condition holds:

$$\frac{\partial p'}{\partial n} = 0 \tag{2.19}$$

where n is the normal to the wall. Through the separation of the variables the solution can be expressed as:

$$p'(\mathbf{x},t) = f(x)g(y)h(z)e^{i\omega t} \tag{2.20}$$

$$\frac{\partial^2 p'}{\partial t^2} = -\omega^2 p' \tag{2.21}$$

$$\frac{\partial^2 p'}{\partial x^2} = -\frac{f''}{f}p'$$

$$\frac{\partial^2 p'}{\partial y^2} = -\frac{g''}{g}p'$$

$$\frac{\partial^2 p'}{\partial z^2} = -\frac{h''}{h}p'$$

Wave equation become:

$$-\frac{\omega^2}{c_0^2} - \frac{f''}{f} - \frac{g''}{g} - \frac{h''}{h} = 0 \tag{2.22}$$

$$\frac{f''}{f} = -\frac{\omega^2}{c_0^2} - \frac{g''}{g} - \frac{h''}{h}$$

$$f'' + \alpha_1^2 f = 0 \tag{2.23}$$

The solution will be in the form:

$$f(x) = A_1 \cos(\alpha_1 x) + B_1 \sin(\alpha_1 x) \tag{2.24}$$

$$\frac{df}{dx}(x) = \alpha_1 \left[-A_1 \sin(\alpha_1 x) + B_1 \cos(\alpha_1 x)\right] \tag{2.25}$$

For the boundary condition: df/dx=0 at x=0 and x=a

$$\begin{cases} B_1 = 0 \\ \sin(\alpha_1 a) = 0 \Rightarrow \alpha_1 a = m\pi \Rightarrow \alpha_1 = m\dfrac{\pi}{a} \end{cases}$$

with m=0,1,2,...

$$f(x) = A_1 \cos\left(m\pi\frac{x}{a}\right) \tag{2.26}$$

Similarly for $g(y)$:

$$g(y) = A_2 \cos\left(n\pi\frac{y}{a}\right) \tag{2.27}$$

with n=0,1,2,...

Instead for $h(z)$: with $f''/f = -m^2\pi^2/a^2$ and $g''/g = -n^2\pi^2/a^2$

$$\frac{d^2 h}{dz^2} + \left[\frac{\omega^2}{c_0^2} - \frac{\pi^2}{a^2}(m^2 + n^2)\right] h \tag{2.28}$$

$$h(z) = A_{mn}e^{-iK_{mn}z} + B_{mn}e^{iK_{mn}z} \tag{2.29}$$

with wavenumber (different from free-field wavenumber):

$$K_{mn} = \sqrt{\frac{\omega^2}{c_0^2} - \frac{\pi^2}{a^2}(m^2+n^2)} \tag{2.30}$$

If $A_1 = A_2 = 0$ the solution can be expressed as follow:

$$p'_{mn}(\mathbf{x},t) = \cos\left(m\pi\frac{x}{a}\right)\cos\left(n\pi\frac{y}{a}\right)\left[A_{mn}e^{i(\omega t - K_{mn}z)} + B_{mn}e^{i(\omega t + K_{mn}z)}\right] \tag{2.31}$$

Each mode thus propagates harmonically in time and in t ans z with both regressive and progressive waves and with the wavenumber K_{mn}. Only in the case where K_{mn} is real do we have wave propagation of the mode:

$$\omega a > \pi c_0\sqrt{m^2+n^2} \tag{2.32}$$

$$\omega a = \pi c_0\sqrt{m^2+n^2} \Rightarrow f_{co} = \frac{c_0}{2a}\sqrt{m^2+n^2} \tag{2.33}$$

$$f = \frac{c_0}{2\pi}\sqrt{K_{mn}^2 + \frac{\pi^2}{a^2}(m^2+n^2)} \tag{2.34}$$

f_{co} is called cut-off frequency:

- If $f > f_{co}$ mode (m,n) propagates
- If $f < f_{co}$ mode (m,n) decays exponentially. These waves are called evanescent waves.

The mode (0,0) is a plane wave. Note that in this case, $f_{co} = 0$, so plane waves always propagate, as f increases a new (m, n) mode begins to propagate . Additionally, note that the decay of the mode is not associated with energy dissipation; instead, energy is transferred to propagating modes after a transient.
For a given f the general solution will have only a finite number of propagating modes and it is of the form:

$$p'(\mathbf{x},t) = \sum_{m=0}^{m=\infty}\sum_{n=0}^{n=\infty} p'_{mn}(\mathbf{x},t) \tag{2.35}$$

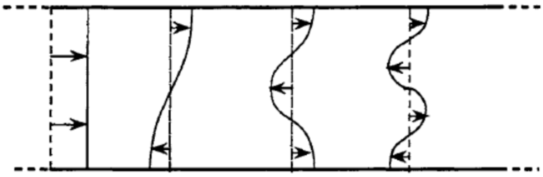

Figure 2.8: Transverse distributions of pressure along a rectangular duct [16]

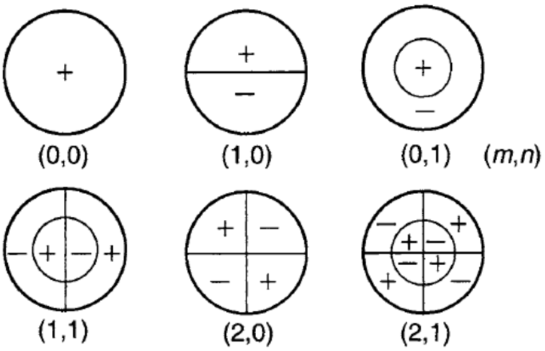

Figure 2.9: Regions of uniform phase in a cylindrical duct [16]

In the specific case of propagation inside a cylindrical duct, m is defined as the ”azimuthal order” or ”circumferential order” and n as the ”radial order” (figure 2.9).

2.4 Far field Analysis

For the evaluation of far-field acoustic emission, once the harmonic steady-state is reached, Actran DGM solves the Ffowcs-Williams and Hawkings equation based on the results obtained in the near-field (section 2.5.2). The following FWH equation can be derived by considering a moving surface S_t, which in our case is a surface including the near-field, moving uniformly with respect to a fixed frame but stationary in the reference frame [1]:

$$4\pi p'(x) = \int_{S_t} (\frac{e^{\frac{-i\omega}{c_0} r_\beta}}{r_\beta(1+M_r)^2} \frac{(i\omega - c_0(M_r + ||\mathbf{M}||^2)}{r_\beta(1+M_r))}(U_n + \frac{L_r}{c_0}) + \frac{L_r + L_m}{r_\beta}) dS_t(\hat{x}) \tag{2.36}$$

with:

- x and $\hat{x}$ are the observer and source position, respectively,
- R = x - $\hat{x}$ is the vector in the radiation direction, and $\mathbf{n} = \frac{\mathbf{R}}{||\mathbf{R}||}$ is its corresponding norm,
- $M_0 = \frac{\mathbf{u_0}}{c_0}$ is the local Mach number vector of the source,
- β is defined by $\beta^2 = 1 - M^2$.

and introducing the following variables:

$$r_\beta = (\frac{\mathbf{R}\cdot\mathbf{u_0}}{c_0} + \sqrt{\frac{(\mathbf{R}\cdot\mathbf{u_0})^2}{c_0^2} + \beta^2||\mathbf{R}||})/\beta^2 \tag{2.37}$$

$$\mathbf{r} = \mathbf{R} - r_\beta \mathbf{M_0} \tag{2.38}$$

$$u_{0n} = \mathbf{u_0}\cdot\mathbf{n} \tag{2.39}$$

$$\hat{u}'_n = \hat{\mathbf{u}}'\cdot\mathbf{n} \tag{2.40}$$

$$U_n = \rho_0 \hat{u}'_n + \hat{\rho}' u_{0n} \tag{2.41}$$

$$\mathbf{L} = \hat{p}'\mathbf{n} + \rho_0 u_{0n}\hat{\mathbf{u}}' \tag{2.42}$$

$$L_m = \mathbf{L}\cdot\mathbf{M_0} \tag{2.43}$$

$$L_r = \mathbf{L}\cdot\frac{\mathbf{r}}{r_\beta} \tag{2.44}$$

$$M_r = \mathbf{r}/r_\beta \cdot \mathbf{M_0} \tag{2.45}$$

Where $\hat{p}'(\hat{x})$, $\hat{\rho}'(\hat{x})$, $\hat{\mathbf{u}}'(\hat{x})$ are the acoustic pressure, velocity and density variables on the moving surface at the source position $\hat{x}$ and c_0, $\mathbf{u_0}$, ρ_0 the constant static mean velocity, density and speed of sound in the far field. By solving this equation, we can obtain the value of $p'(x)$ at every point in the far field.

2.5 Acoustic Analogies

2.5.1 Lighthill Analogy

In 1952, Lighthill developed an acoustic analogy based on the recombination of the Navier-Stokes equations [5]:

$$\begin{cases} \dfrac{\partial p'}{\partial t} + \dfrac{\partial(\rho u_i)}{\partial x_i} = 0 \\ \dfrac{\partial(\rho u_i)}{\partial t} + \dfrac{\partial \rho u_i u_j}{\partial x_i} = \dfrac{\partial \sigma_{ij}}{\partial x_j} \end{cases} \tag{2.46}$$

where $\sigma_{ij} = -p\delta_{ij} + \tau_{ij}$. The effects of heat are neglected by not considering the energy equation. By differentiating the continuity equation with respect to t and the conservation of momentum equation with respect to x_i:

$$\begin{cases} \dfrac{\partial^2 p'}{\partial t^2} + \dfrac{\partial^2(\rho u_i)}{\partial t \partial x_i} = 0 \\ \dfrac{\partial^2(\rho u_i)}{\partial t \partial x_i} + \dfrac{\partial^2(\rho u_i u_j - \sigma_{ij})}{\partial x_i \partial x_j} \end{cases} \tag{2.47}$$

Subtracting the second equation of the system from the first:

$$\frac{\partial^2 p'}{\partial t^2} = \frac{\partial^2(\rho u_i u_j - \sigma_{ij})}{\partial x_i \partial x_j} \tag{2.48}$$

Subtracting $c_0^2 \frac{\partial^2 \rho}{\partial x_i \partial x_j} \delta_{ij}$ from both sides:

$$\frac{\partial^2 p'}{\partial t^2} - c_0^2 \frac{\partial^2 \rho}{\partial x_i \partial x_j} \delta_{ij} = \frac{\partial^2(\rho u_i u_j - \sigma_{ij})}{\partial x_i \partial x_j} - c_0^2 \frac{\partial^2 \rho}{\partial x_i \partial x_j} \delta_{ij} \tag{2.49}$$

$$\frac{\partial^2 \rho}{\partial t^2} - c_0^2 \frac{\partial^2 (\rho u_i)}{\partial x_i \partial x_j} \delta_{ij} = \frac{\partial^2 (\rho u_i u_j + (p - c_0^2 \rho)\delta_{ij} - \tau_{ij})}{\partial x_i \partial x_j} \tag{2.50}$$

Defining fluctuations with respect to a reference state with constant properties $p_0 = cost$, $\rho_0 = cost$ and at rest $u_0 = 0$

$$\begin{cases} p' = p - p_0 \\ \rho' = \rho - \rho_0 \\ u_i' = u_i - u_{i_0} \end{cases}$$

Lighthill equation is obtained:

$$\frac{\partial^2 \rho}{\partial t^2} - c_0^2 \frac{\partial^2 (\rho u_i)}{\partial x_i \partial x_j} \delta_{ij} = \frac{\partial^2 T_{ij}}{\partial x_i \partial x_j} \tag{2.51}$$

where $T_{ij} = \rho u_i u_j + (p - c_0^2 \rho)\delta_{ij} - \tau_{ij}$ is the *Lighthill Tensor* which implicitly contains all the sound generation effects within it. This equation is exact because derived from a simple reformulation of the Navier-Stokes equations and not from a linearization. It cannot be treated as a classical wave equation because the right-hand term contains the acoustic field and cannot simply be considered a source term. The equation cannot be explicitly solved using the formalism of Green's functions, to do so, Some approximations are made under conditions of low Mach and high Reynolds numbers:

- Mechanical actions dominate over viscous effects: $\tau_{ij} << \rho u_i u_j$
- Mechanical actions dominate over thermal effects $p' - c_0^2 \rho' = 0$
- For small Mach numbers $\rho \approx \rho_0$

therefore:

$$T_{ij} \approx \rho_0 u_i u_j. \tag{2.52}$$

Lighthill equation is now explicit:

$$\frac{\partial^2 \rho}{\partial t^2} - c_0^2 \frac{\partial^2 (\rho u_i)}{\partial x_i \partial x_j} \delta_{ij} = \frac{\partial^2 (\rho_0 u_i u_j)}{\partial x_i \partial x_j} \tag{2.53}$$

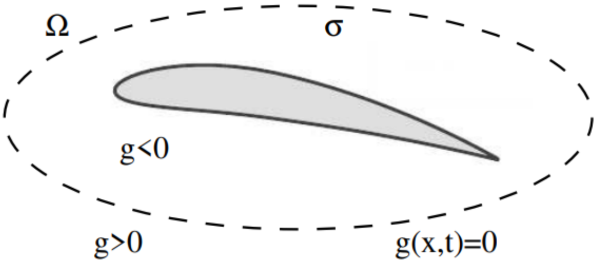

Figure 2.10: Ffowcs Williams & Hawkings Surface[5]

Now it is possible to solve the non-homogeneous wave equation using the Green's functions technique:

$$c_0^2\rho'(\mathbf{x},t) = c_0^2(\rho(\mathbf{x},t)-\rho_0) = \frac{1}{4\pi}\frac{\partial^2}{\partial x_i \partial x_j}\int_{\Omega_S}\frac{T_{ij}\left(\mathbf{y},t-\frac{|\mathbf{x}-\mathbf{y}|}{c_0}\right)}{|\mathbf{x}-\mathbf{y}|}\mathbf{dy} \tag{2.54}$$

However, the simplifications lead to the absence of feedback. Indeed, since the source term is expressed only as a function of the Reynolds tensor and not also of the acoustic fluctuations, the acoustic and fluid dynamics fields are decoupled.

2.5.2 Ffowcs Williams & Hawkings Analogy

Is possible to extend the Lighthill analogy to the case of a moving body obtaining the formulation of Ffowcs Williams & Hawkings .
It is assumed that the acoustic field is identically zero inside σ_y, and this is enforced through the following formalism (figure 2.10) [5]:

$$H(g) = \begin{cases} 0 & \text{inside } \sigma \quad (g<0) \\ 1 & \text{outside } \sigma \quad (g>0) \end{cases}$$

The constant value $g = 0$ follows the motion of the surface σ_y:

$$\frac{Dg}{Dt} = \frac{\partial g}{\partial t} + U_i \frac{\partial g}{\partial x_i} = 0 \tag{2.55}$$

Multiplying the balance equations by H(g):

$$\begin{cases} H(g)[\frac{\partial \rho}{\partial t} + \frac{\partial(\rho u_i)}{\partial x_i}] \\ H(g)[\frac{\partial(\rho u_i)}{\partial t} + \frac{\partial(\rho u_i u_j - \sigma_{ij})}{\partial x_j}] \end{cases} \tag{2.56}$$

$$\begin{aligned}
&\delta(g) = \frac{\partial H}{\partial g} \Rightarrow \frac{\partial H}{\partial t} = \delta(g)\frac{\partial g}{\partial t} \text{ e } \frac{\partial H}{\partial x_i} = \delta(g)\frac{\partial g}{\partial x_i} : \\
&H(g)\left[\frac{\partial}{\partial t}(\rho - \rho_0) + \frac{\partial}{\partial x_i}(\rho u_i)\right] = 0, \\
&\frac{\partial}{\partial t}[(\rho - \rho_0)H] + \frac{\partial}{\partial x_i}[\rho u_i H] = (\rho - \rho_0)\frac{\partial H}{\partial t} + \rho u_i \frac{\partial H}{\partial x_i}, \\
&\frac{\partial}{\partial t}[(\rho - \rho_0)H] + \frac{\partial}{\partial x_i}[\rho u_i H] = (\rho - \rho_0)\frac{\partial g}{\partial t}\delta(g) + \rho u_i \frac{\partial g}{\partial x_i}\delta(g), \\
&\frac{\partial}{\partial t}[(\rho - \rho_0)H] + \frac{\partial}{\partial x_i}[\rho u_i H] = \underbrace{[\rho\,(u_i - U_i) + \rho_0 U_i]\,\frac{\partial g}{\partial x_i}\delta(g)}_{Q_m \delta(g)}.
\end{aligned}$$

The continuity equation becomes a continuity equation with variables that are zero inside sigma since they are now multiplied by H. Additionally, a source term Q_m has appeared on the right-hand side of the equation, localized on the surface as it is multiplied by the $\delta(g)$ function. $\delta(g) = \frac{\partial H}{\partial g} = 0$ everywhere except at the crossing of σ_y, where it goes to infinity. This corresponds to the Dirac delta function.

Q_m can be interpreted as a distribution of mass sources:

$$Q_m = [\rho(u_i - U_i + \rho_0 U_i]\frac{\partial g}{\partial x_i} \tag{2.57}$$

Similarly, in the momentum equation, a force surface distribution of force on sigma is obtained on σ_y:

$$F_i = u_i Q_m + \rho_0 f_i \tag{2.58}$$

with:

$$\rho_0 f_i = -[\rho_0 u_i U_j + \sigma_{ij} + p_0 \delta_{ij}]\frac{\partial g}{\partial x_i} \tag{2.59}$$

$$\begin{cases} \dfrac{\partial[(\rho-\rho_0)H]}{\partial t}+\dfrac{\partial[\rho u_i H]}{\partial x_i}=Q_m\delta(g) \\ \dfrac{\partial[\rho u_i H]}{\partial t}+\dfrac{\partial[(\rho u_i u_j-\sigma_{ij}-p_0\delta_{ij})H]}{\partial x_i}=F_i\delta(g) \end{cases} \tag{2.60}$$

By differentiating the first equation with respect to time, taking the divergence of the second, and subsequently subtracting the second equation from the first:

$$\begin{aligned} \frac{\partial^2}{\partial t^2}[(\rho-\rho_0)H] &= \frac{\partial}{\partial t}(Q_m\delta(g))-\frac{\partial}{\partial x_i}(F_i\delta(g)) \\ &+\frac{\partial^2}{\partial x_i\partial x_j}\left[\left(\rho u_i u_j-\sigma_{ij}-p_0\delta_{ij}\right)H\right] \end{aligned} \tag{2.61}$$

$$\begin{aligned} \frac{\partial^2}{\partial t^2}\left(\rho' H\right)-c_0^2\frac{\partial^2}{\partial x_i\partial x_i}\left(\rho' H\right) &= \frac{\partial}{\partial t}(Q_m\delta(g))-\frac{\partial}{\partial x_i}(F_i\delta(g)) \\ &+\frac{\partial^2}{\partial x_i\partial x_j}\left[\left(\rho u_i u_j-\sigma_{ij}-p_0\delta_{ij}-c_0^2\rho'\delta_{ij}\right)H\right] \end{aligned} \tag{2.62}$$

$$\begin{cases} -\sigma_{ij}-p_0\delta_{ij}=-\tau_{ij}+p\delta_{ij}-p_0\delta_{ij}=-\tau_{ij}+p'\delta_{ij} \\ T_{ij}=\rho u_i u_j-\tau_{ij}+\left(p'-c_0^2\rho'\delta_{ij}\right) \end{cases} \tag{2.63}$$

Finally, FWH equation is obtained.This equation represents an extension of the Lighthill equation in the case where the sought solution is nonzero only outside the moving surface σ_y. Compared to before, the presence of the moving boundary results in the appearance of two additional source terms on the right-hand side of the equation:

$$\frac{\partial^2[\rho' H(g)]}{\partial t^2}-c_0^2\frac{\partial^2[\rho' H(g)]}{\partial x_i\partial x_j}=\frac{\partial Q_m\delta(g)}{\partial t}-\frac{\partial(F_i\delta(g))}{\partial x_i}+\frac{(T_{ij}H(g))}{\partial x_i\partial x_j} \tag{2.64}$$

Also in this case, the formalism of Green's functions can be used for the solution of the equation:

$$\begin{aligned} H(g)c_0^2\rho'(\mathbf{x},t) &= \int_{-\infty}^{\infty}\int_{\Omega_\infty}G_0\left[\frac{\partial}{\partial\tau}(Q_m\delta(g))-\frac{\partial}{\partial y_i}(F_i\delta(g))\right. \\ &\left.+\frac{\partial^2}{\partial y_i\partial y_j}\left(T_{ij}H(g)\right)\right]\mathrm{d}\mathbf{y}\mathrm{d}\tau \end{aligned} \tag{2.65}$$

where:

$$G_0 = \frac{1}{4\pi|\mathbf{x}-\mathbf{y}(\tau)|}\delta\left(t-\tau-\frac{|\mathbf{x}-\mathbf{y}(\tau)|}{c_0}\right) \tag{2.66}$$

$$\begin{aligned} H(g)c_0^2\rho'(\mathbf{x},t) =& \frac{1}{4\pi}\frac{\partial^2}{\partial x_i \partial x_j}\int_{\Omega(t^*)}\left[\frac{T_{ij}}{R|1-M_\sigma\cos\theta|}\right]_{t^*}\mathrm{d}\mathbf{y} \\ &+\frac{1}{4\pi}\frac{\partial}{\partial t}\int_{\sigma(t^*)}\left[\frac{\rho_0 U_i+\rho\left(u_i-U_i\right)}{R|1-M_\sigma\cos\theta|}\right]_{t^*} n_i\,\mathrm{d}\sigma \\ &-\frac{1}{4\pi}\frac{\partial}{\partial x_i}\int_{\sigma(t^*)}\left[\frac{\rho u_i\left(u_j-U_j\right)-\sigma_{ij}}{R|1-M_\sigma\cos\theta|}\right]_{t^*} n_j\,\mathrm{d}\sigma. \end{aligned} \tag{2.67}$$

In far field: $c_0^2\rho' = p', [R]_{t^*} \approx R, \frac{\partial}{\partial x_i} \approx -\frac{x_i}{R}\frac{1}{c_0}\frac{\partial}{\partial t}$ e $H=1$

$$\begin{aligned} p'(\mathbf{x},t) \approx& \frac{1}{4\pi c_0^2}\frac{x_i x_j}{R^3}\frac{\partial^2}{\partial t^2}\int_{\Omega(t^*)}\left[\frac{T_{ij}}{|1-M_\sigma\cos\theta|}\right]_{t^*}\mathrm{d}\mathbf{y} \\ &+\frac{1}{4\pi R}\frac{\partial}{\partial t}\int_{\sigma(t^*)}\left[\frac{\rho_0 U_i+\rho\left(u_i-U_i\right)}{|1-M_\sigma\cos\theta|}\right]_{t^*} n_i\,\mathrm{d}\sigma \\ &+\frac{1}{4\pi c_0}\frac{x_i}{R^2}\frac{\partial}{\partial t}\int_{\sigma(t^*)}\left[\frac{\rho u_i\left(u_j-U_j\right)-\sigma_{ij}}{|1-M_\sigma\cos\theta|}\right]_{t^*} n_j\,\mathrm{d}\sigma. \end{aligned} \tag{2.68}$$

The first term is a quadrupole and is the cause of ”turbulence noise” generated by turbulent structures rearranging. The volume integral is very challenging to solve numerically. Typically, one attempts to extend the surface sigma so that it encompasses all fluid motion, incorporating all effects into the monopole and dipole, which are the second and third terms, respectively. These are the causes of ”thickness noise,” determined by the accelerated movement of the body, and ”loading noise,” determined by fluctuations of force exchanged between the body and fluid.

Chapter 3

Validation

In turn to validate the numerical Actran set-up preliminary simulation, for which the solution is known, have been run. The selected engine for validation and subsequent analysis is the *Pratt&Whitney* Canada JT15D (figure 3.1).
The JT15D is a turbofan engine with a nominal bypass ratio of 3.3 and a thrust of 9790 N. The fan features 28 blades and a diameter of 53.5 cm [26].
It was chosen for:

- Extremely simple engine geometry.
- By design, the inlet geometry and the blade passage frequency support only one propagating mode with m = 13 and n = 1 [39].
- The test is conducted under static conditions.
- The availability of experimental data, both with and without liner, enables verification that the numerical attenuation effect of the liner is consistent with the experimental results.

Experimental acoustic emission values have been investigated at the NASA Lewis Vertical Lift Facility to develop finite difference and finite element programs for simulating sound propagation in turbofan engines. To reduce turbulence and distortion in the inlet flow, a spherical inflow control screen covering the inlet was employed. Additionally, a large muffler was connected to the engine exhaust to suppress after-fan and jet noise (figure 3.2). The engine was mounted 5.4 fan diameters above the ground to minimize its

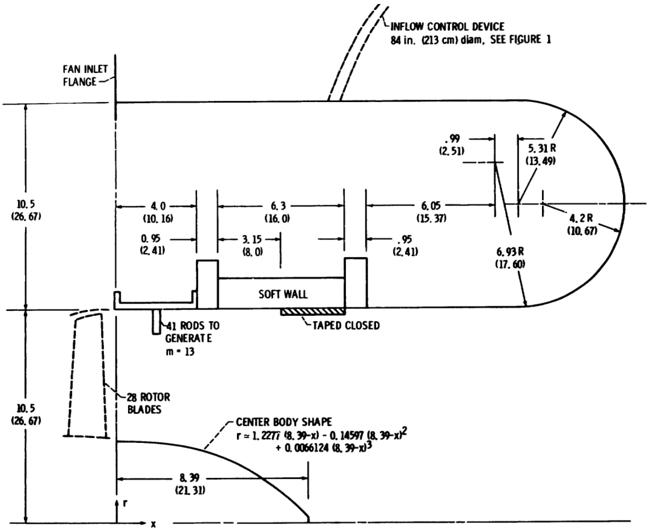

Figure 3.1: Detailed geometry of JT15D engine inlet [26]

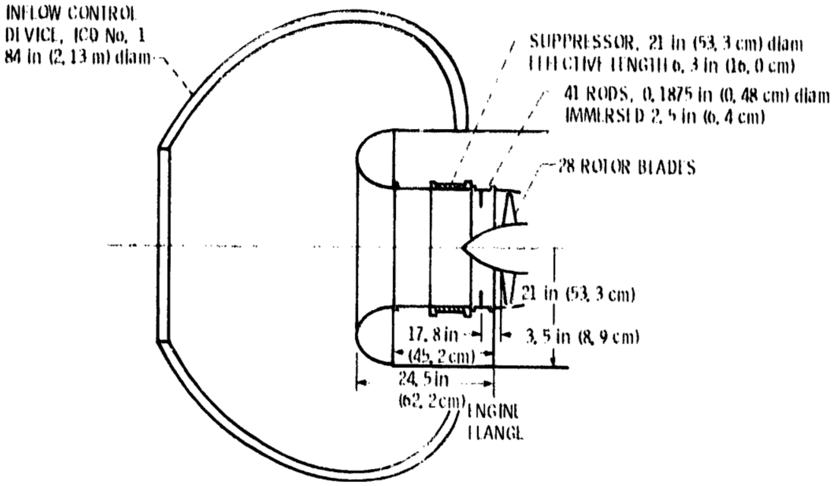

Figure 3.2: Test Configuration [27]

Table 3.1: Experimental Relative SPL [dB] values at 24.38m and 3150Hz

	40	50	60	70	80	90
Hard Wall	91.6	99.0	100.0	99.1	93.4	89.1
With Liner		81.3	82.2	78.6	73.6	

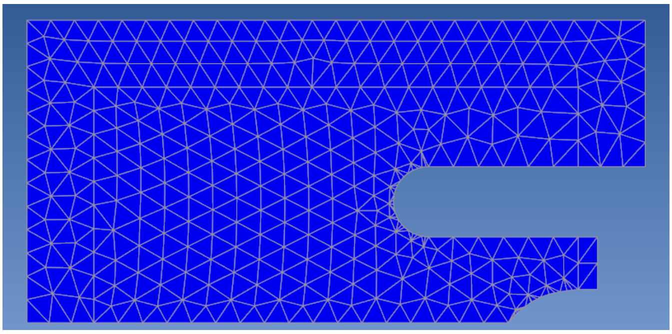

Figure 3.3: Acoustic mesh

effect [26]. The microphones signals were recorded on magnetic tape and the processed on a spectrum analyzer [27]. Sound Pressure Level (SPL) results were obtained for a microphone array positioned 24.38 meters from the inlet at a blade passage frequency of 3150 Hz. The data were then normalized so that the value at the microphone positioned 60° relative to the engine axis was set to 100 dB (table 3.1). The evaluation was conducted for both a hard wall case, without liner, and a case with acoustic treatment, with an estimated impedance value of 1.136 + 0.5i and a liner extension of 3.15”. The model used for impedance calculation is reported in [28].

3.1 Simulation set-up and validation results

Firstly, the 2D engine CAD was imported in IGES format into Actran. Afterward, the acoustic mesh was generated (figure 3.3), following the aforementioned criteria. The analysis was set for a frequency of 3150 Hz (multiple frequencies could be set), and it was configured as axisymmetric to save computation time. However, this limited the injection of modes to those with the same azimuthal order. Then, the geometry was divided into domains, and each domain was assigned to its component and/or boundary condition. Specifically, all simulations injected the acoustic mode (13,1) with

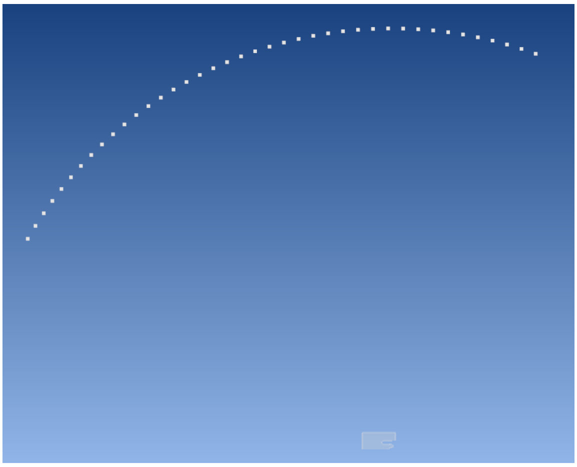

Figure 3.4: Microphones distribution

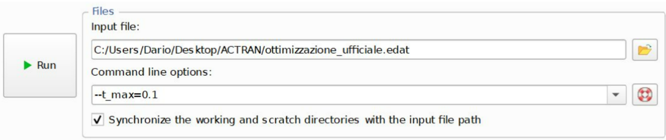

Input file: C:/Users/Dario/Desktop/ACTRAN/ottimizzazione_ufficiale.edat

Command line options: --t_max=0.1

☑ Synchronize the working and scratch directories with the input file path

Figure 3.5: Run simulation

an intensity of $1W/m^2$ into the modal component. Since the real amplitude of the acoustic mode is unknown, this value serves as a reference. Finally, an array of 40 microphones was positioned from 40° to 110° relative to the engine axis and at a distance of 24.48m (figure 3.4).

With this setup complete, the simulation could be launched (figure 3.5). Examining the obtained results, it can be concluded that the experimental and numerical data demonstrate a good degree of agreement, both concerning the directivity of the acoustic emission and the achieved attenuation (figure 3.6).

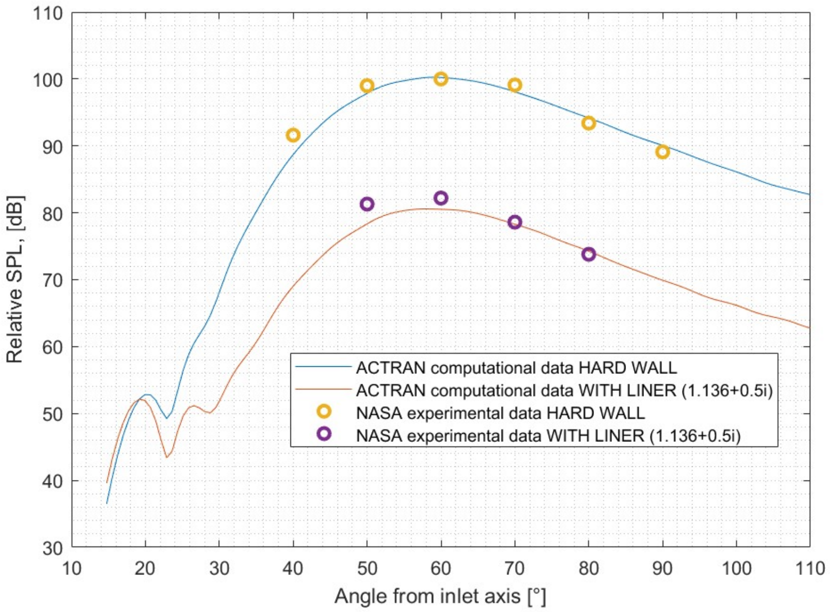

Figure 3.6: Comparison between experimental and numerical data at 24.28 m [3150 Hz]

Chapter 4

Results and discussion

Initially, three analyses were conducted in the absence of flow: one without a liner, one with SDoF liner, and one with DDoF liner, aiming to evaluate the achievable attenuation with a non-optimized acoustic treatment. The impedance model used is the Motsinger and Kraft Model, and the model parameters used are listed in tables 4.1 and table 4.2, chosen based on typical literature values. It was chosen not to start from geometric values that already determined a resonance condition at 3150 Hz in order to generalize the optimization process starting from an initial condition that disregarded any previous evaluations and to highlight the importance of the cavity depth in achieving resonance conditions and minimizing acoustic emission.
By plotting the impedance modulus curve against frequency for this non-optimized condition, it is observed that the representative minima of the resonance condition do not coincide with the frequency of 3150 Hz (figure

Table 4.1: SDoF model parameters for *h* and *d* optimization

h [m]	0.004
d [m]	0.0012
σ [%]	28
t [m]	0.002
f [Hz]	3150
c [m/s]	343
μ $[Pa \cdot s]$	1.716×10^{-5}
$\rho [kg/m^3]$	1.225
C_d	0.76
Normalized Impedance	0.00852 + 1.4503i

Table 4.2: DDoF model parameters

h_1 [m]	0.02
h_2 [m]	0.0012
d_1 [m]	0.02
d_2 [m]	0.0012
σ_1 [%]	28
σ_2 [%]	28
t [m]	0.002
f [Hz]	3150
c [m/s]	343
$\mu\ [Pa \cdot s]$	1.716×10^{-5}
$\rho [kg/m^3]$	1.225
C_d	0.76
Normalized Impedance	0.0251 +1.1799i

4.1 and 4.25), which is the frequency we aim to minimize the generated noise. Therefore, it is expected that after optimization, these valleys will coincide with the frequency of 3150 Hz, resulting in an increase in attenuation.

An improvement of approximately 12 dB is observed compared to the case without a liner (figure 4.3), with a slightly more attenuated curve for the DDoF case. This attenuation is also evident when comparing the two pressure fields in the absence and presence of the SDoF liner , showing a reduction in acoustic oscillation at the location of the liner in the bypass duct. In figure 4.4 and figure 4.5, the pressure fields in the absence and presence of the SDoF acoustic liner at the pre-optimized impedance value are shown. These fields result from injecting mode (13,1) with an amplitude of $1W/m^2$ into the bypass duct in the case of no flow. The color scale for visualizing the acoustic oscillation relative to the reference value of 101325, taken as 0, has been limited to [+5 Pa; -5 Pa] in order to better highlight the attenuation effect of the liner.

4.1 Flow effect

In order to assess the effect of flow on far-field results and subsequently on optimization parameters, the iCFD (integrated Computational Fluid Dynamics) module of Actran was used to interpolate the fluid dynamics field, previously calculated on an external CFD code, onto the acoustic mesh.

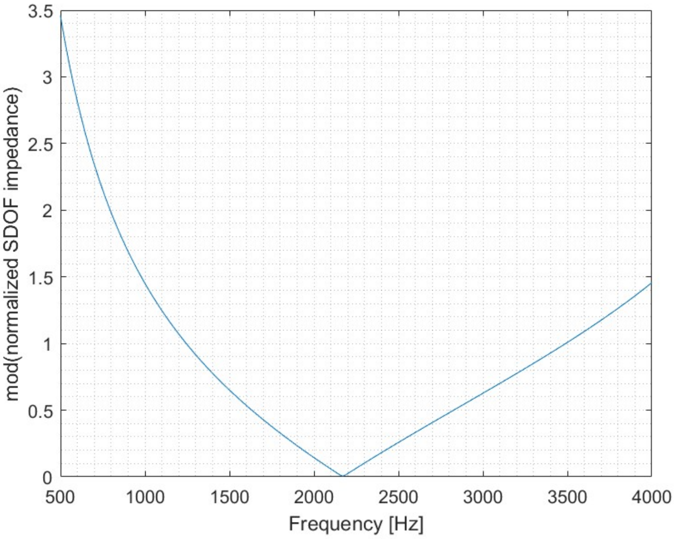

Figure 4.1: Non optimized impedance modulus for SDoF liner

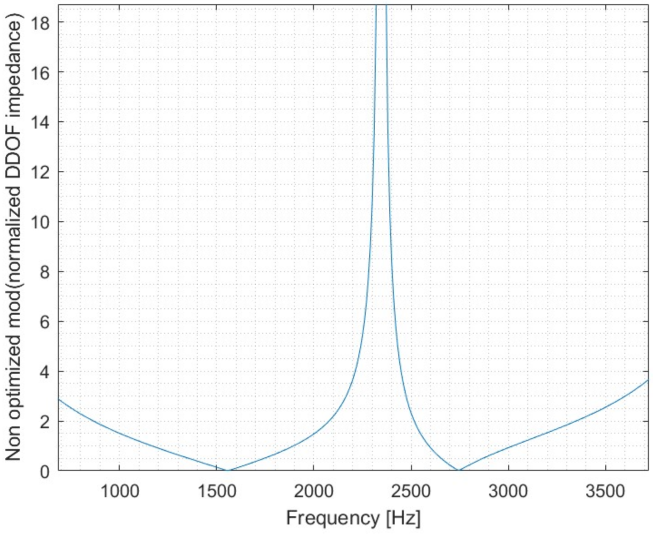

Figure 4.2: Non optimized impedance modulus for DDoF liner

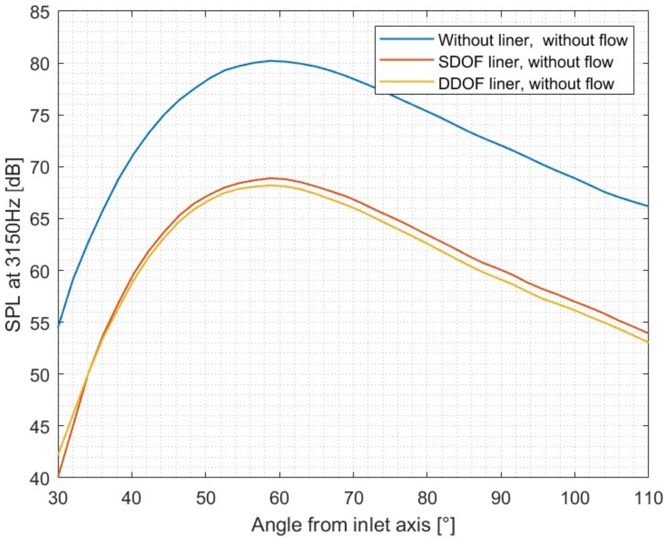

Figure 4.3: Attenuation effect of SDoF and DDoF liners in the absence of flow

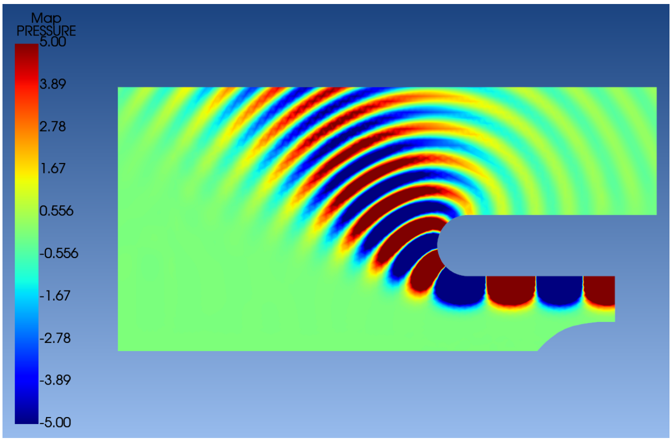

Figure 4.4: Limited pressure field [5 Pa ; -5 Pa] without liner

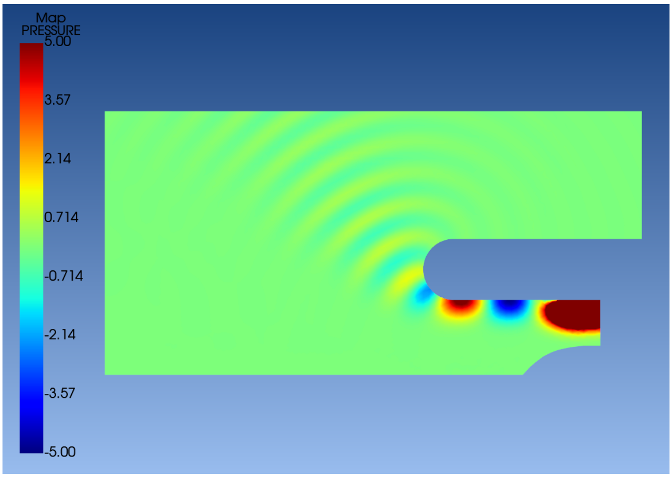

Figure 4.5: Limited pressure field [5 Pa; -5 Pa] with SDoF liner

4.1.1 CFD analysis

To solve the fluid dynamics field, Star-CCM+ was chosen. Star-CCM+ is a CFD calculation software developed by *CD-Adapco* and widely used both in academic and industrial settings for solving engineering problems through the solution of the Navier-Stokes equations using the finite volume method. The internal CAD tool within STAR-CCM+ was utilized to create the engine geometry. Subsequently, *parts* and *regions* (figure 4.7) were generated:

- **Inlet:** Stagnation Inlet
- **Outlet 2:** Pressure Outlet
- **Outlet 1:** Velocity Inlet
- **Engine:** Wall
- **Up:** Symmetry Plane
- **Down:** Symmetry Plane

Given the unavailability of the actual JT15D fan geometry, a 3D simulation was not conducted. Instead, a representative axisymmetric simulation under static engine operation conditions was established. To simulate the fan suction effect, an outlet velocity equal to Mach=0.15 was set at the fan section. Although this simulation does not precisely replicate the real fluid dynamics

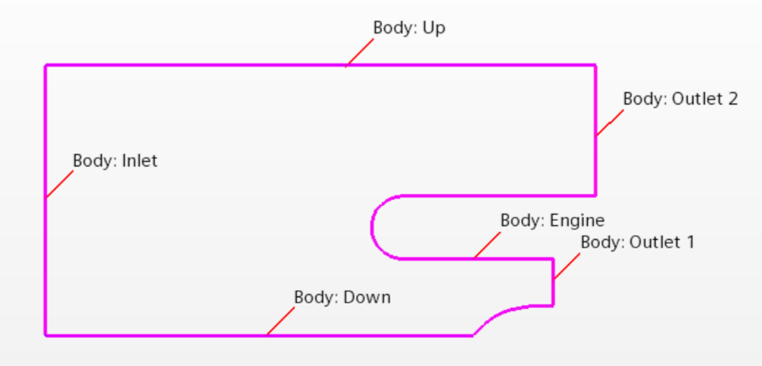

Figure 4.6: CFD boundary conditions

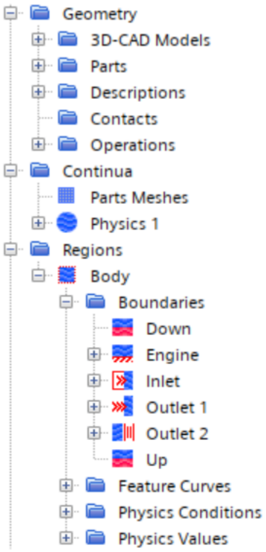

Figure 4.7: CFD regions definition

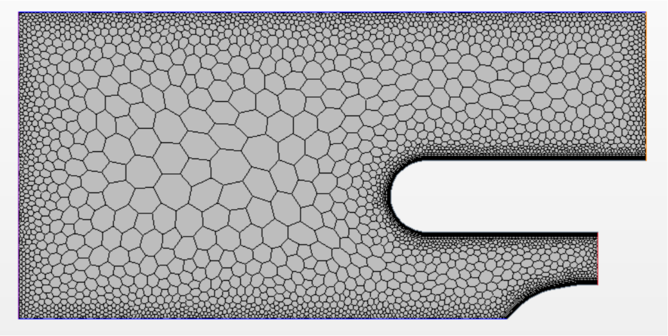

Figure 4.8: CFD Mesh

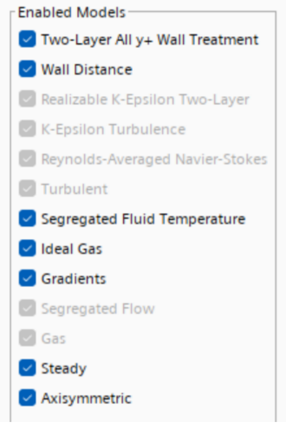

Enabled Models

- ☑ Two-Layer All y+ Wall Treatment
- ☑ Wall Distance
- ☑ Realizable K-Epsilon Two-Layer
- ☑ K-Epsilon Turbulence
- ☑ Reynolds-Averaged Navier-Stokes
- ☑ Turbulent
- ☑ Segregated Fluid Temperature
- ☑ Ideal Gas
- ☑ Gradients
- ☑ Segregated Flow
- ☑ Gas
- ☑ Steady
- ☑ Axisymmetric

Figure 4.9: CFD physiscs

field within the bypass duct, it still offers a credible description suitable for assessing the impact of flow on the outcomes of the aeroacoustic simulation in Actran. The fluid dynamics mesh (figure 4.8) was then developed, and the problem's physics (figure 4.9) were defined as stationary, axisymmetric, utilizing a $k-\varepsilon$ turbulence model.

Once the CFD field was calculated (figure 4.10), the results were exported in Ensight Gold format, compatible with Actran, to import them into Actran's iCFD module, achieving the interpolation of the field on the acoustic mesh (figure 4.11).

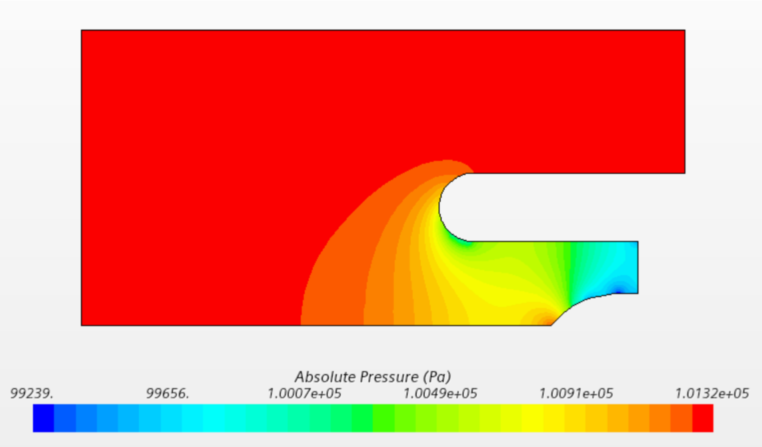

Figure 4.10: CFD pressure field

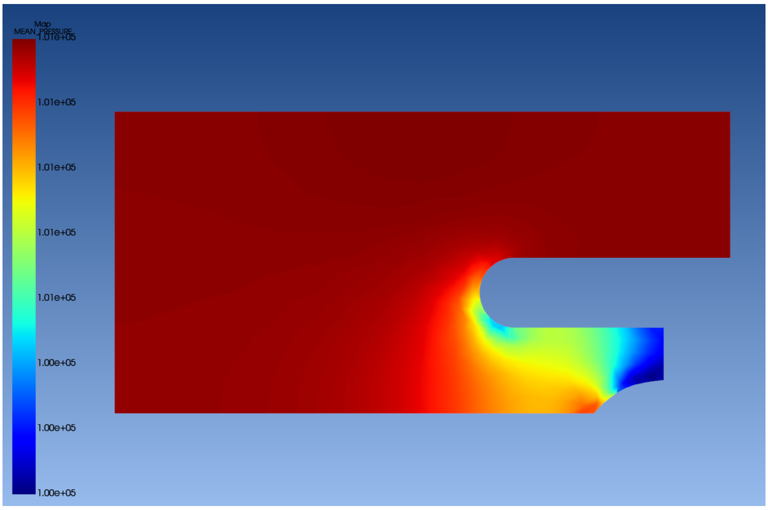

Figure 4.11: Interpolation pressure field on acoustic mesh

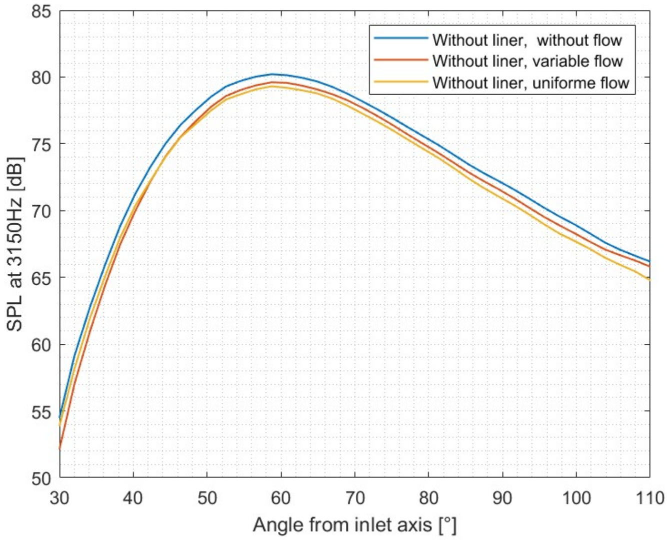

Figure 4.12: Flow effect in the absence of liner

4.1.2 Flow effect results

Therefore, it was possible to compare the results obtained in the absence of flow, in the presence of uniform flow equal to Mach=0.1 throughout the field (a condition specified directly within Actran), and in the presence of the variable flow interpolated from the solution obtained with Star-CCM+. M=0.1 has been chosen since M=0.15 represents the maximum velocity in the bypass duct reached at the fan section, but the velocity distribution in the duct is generally lower on average. The results show that in the absence of an acoustic liner, the effect of the flow is minimal (figure 4.12). The curves representing the three conditions differ by approximately 1dB, with the case without a liner weakly tending to overestimate the SPL.

However, the same cannot be said in the presence of an acoustic liner. Indeed, the effect of the flow in the presence of an SDoF liner is much more pronounced (figure 4.13). The acoustic emission with uniform flow is over 5dB higher than the cases without flow and with variable flow, whose curves are almost overlapping, but with a slightly altered directivity due to the presence of uniform flow.

Finally, in the case of a DDoF liner (figure 4.14), the presence of uniform flow also results in an SPL curve approximately 5dB higher than that without

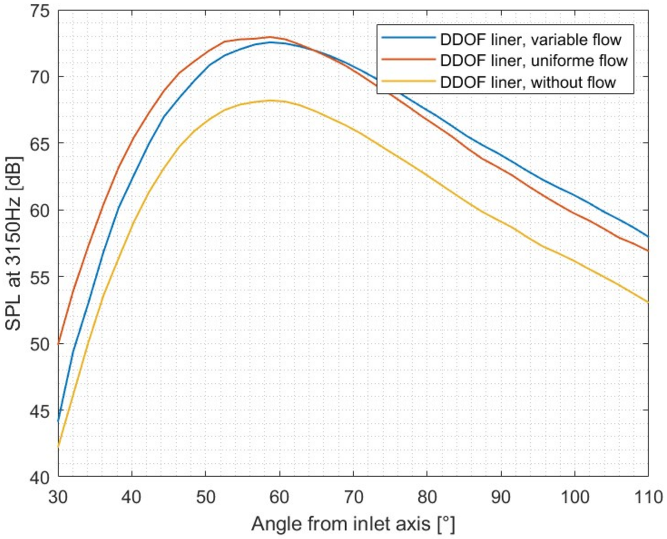

Figure 4.13: Flow effect in the presence of SDoF liner

flow, perceptibly modifying the directivity of the curve in this case as well.

4.2 Optimization

A Python code was developed to allow finding the minimum acoustic emission. Python was chosen because Actran is written in this language, which greatly simplifies coupling the optimization code with the software. Specifically, the Motsinger and Kraft model for an SDoF liner was utilized, initially optimizing only h and d, and subsequently also σ. Additionally, the impact of flow on the optimization results was assessed for this liner. Finally, an optimization was conducted for a DDoF, optimizing h_1, h_2, d_1, and d_2 of the Motsinger and Kraft model.

4.2.1 Optimization approach

Actran contains the Python free/open-source library NLopt, which implements various local and global optimization algorithms, both derivative-free and derivative-based. NLopt also allows limiting the exploration field to search for the optimum by specifying constraints that ensure finding phys-

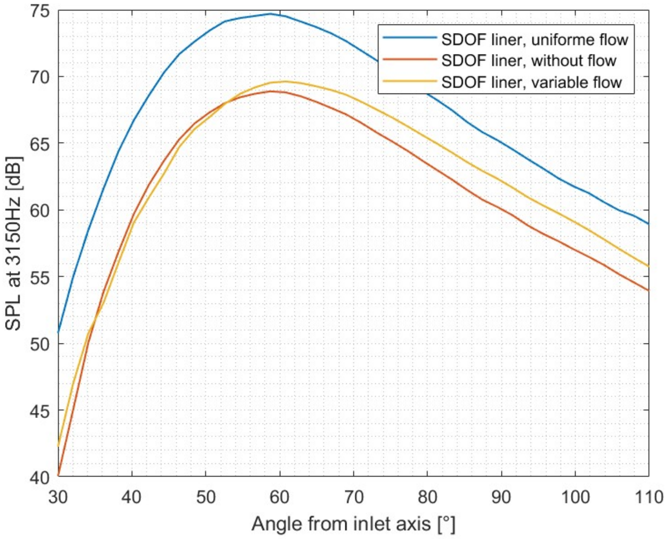

Figure 4.14: Flow effect in the presence of DDoF liner

ically acceptable solutions for the optimization parameters. The chosen optimization strategy involves investigating the most promising areas of minimum acoustic emission by initially employing the global optimization algorithm DIRECT [24]. Subsequently, these areas are further explored using the local optimizer COBYLA [36].

DIRECT DIRECT (DIviding RECTangles) is a global derivative-free optimization algorithm, this makes it particularly suitable for optimization problems in numerical simulations, where the objective function is often non-differentiable [12]. The approach involves subsequent exploration of areas of minimum search in increasingly smaller hyper-rectangles and evaluates the objective function at their center points (figure 4.15). However, the search begins by heating bound constraints to a hypercube, ensuring that all search directions have equal weight.

COBYLA COBYLA (Constrained Optimization by Linear Approximation) is a local derivative-free optimization algorithm. ”It works by iteratively approximating the actual constrained optimization problem, that is, by constructing linear polynomial approximations to the objective and constraint functions. Therefore, during an iteration, an approximating linear program-

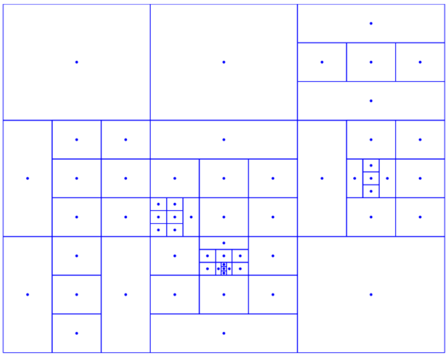

Figure 4.15: Direct optimization approach [24]

ming problem is solved to obtain a candidate for the optimal solution. The candidate solution is evaluated using the original objective and constraint functions, yielding a new data point in the optimization space. This information is used to improve the approximating linear programming problem used for the next iteration of the algorithm" [23].

4.2.2 Optimization results

The optimization was initially carried out for a case with no flow, both for a SDoF liner and a DDoF liner. For both cases, the function chosen to minimize was the average SPL (the average SPL calculated over the 40 microphones along the arc). By doing this, it was decided to give equal weight to all microphones. A different approach could have involved assigning different weights to the various microphones to give more importance to one or another. Furthermore, for both scenarios, the use of a single local optimizer was compared against the sequential use of a global optimizer followed by a local one. Subsequently, the effect of flow was evaluated for SDoF liner optimization. For all optimizations, the values used as the starting point were those with which an initial assessment of attenuation for a non-optimized case was performed. The optimization was initially conducted for scenarios without flow, encompassing both SDoF and DDoF liners. In each case, the objective function selected for minimization was the average SPL, calculated over the 40 microphones along the arc. Furthermore, for both scenarios, the use of a single local optimizer was compared against the sequential use of a global optimizer followed by a local one.

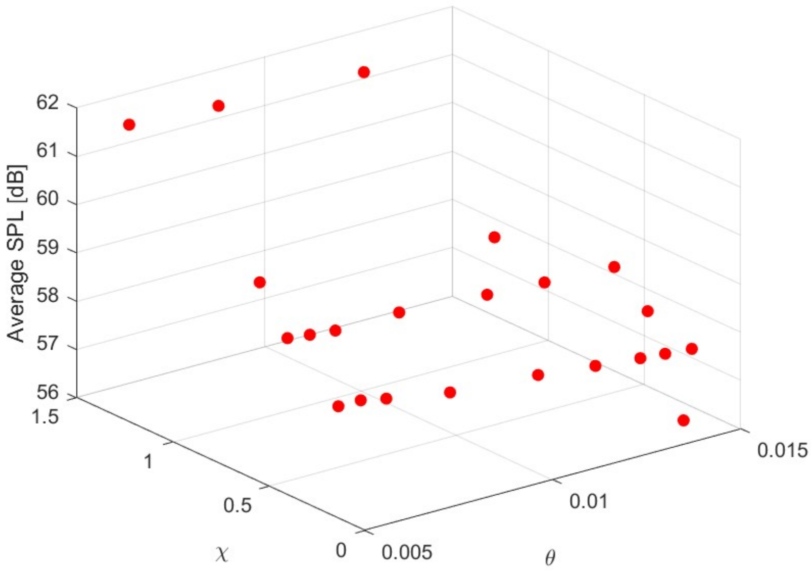

Figure 4.16: Direct SDoF optimization (h, d) values without flow

SDoF without flow

A first optimization, whose results are reported in table 4.3, was performed by optimizing only h and d. Tracking the values during the optimization cycle makes it clear how the optimization algorithm tends to quickly approach resonance conditions by reducing h and moving towards $\chi = 0$, while also reducing d to increase resistance (figure 4.16 and 4.17). This becomes evident by reasoning with the Motsinger and Kraft Model, where reactance is mainly governed by the geometric parameter h and resistance by d (figure 1.25 and 1.26). Hence, this initial optimization problem appears to be very simple, as it is observed that comparing the results obtained using only a

Table 4.3: SDoF optimization results, no flow (h, d)

	Direct+Cobyla	Only Cobyla
h [m]	0.02	0.02
d [m]	0.0009	0.000915
Average SPL [dB]	55.0880	55.1248
Normalized impedance	0.0152 + 0.0678i	0.0147 + 0.0694i

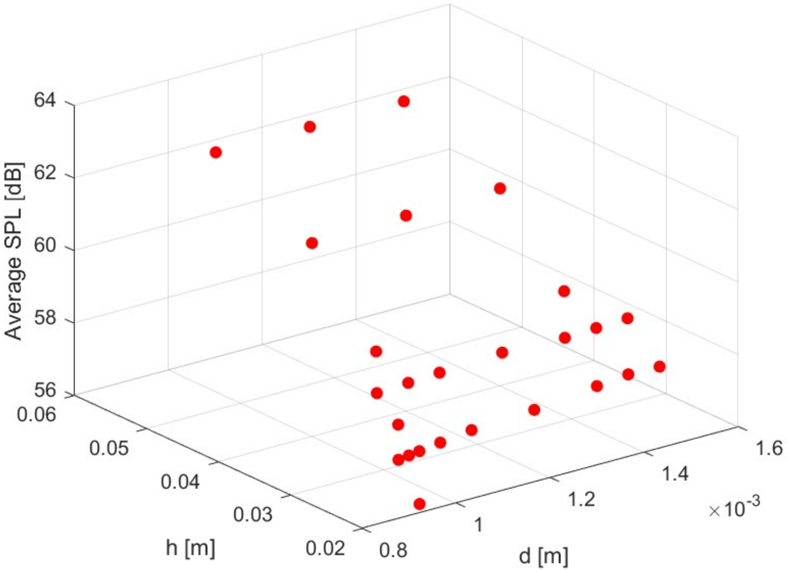

Figure 4.17: Direct SDoF optimization (h,d) values without flow

local optimization algorithm and those obtained by sequentially using a global optimizer to determine the most promising areas and then the local algorithm, they coincide; both values quickly approach the lower limits of the provided physical constraints. On the other hand, this second approach results in a significant increase in the necessary iterations, greatly extending the computation times to find the minimum (figure 4.18).

It should be noted that by plotting the impedance modulus curve with the newly optimized parameters against frequency, the valley aligns precisely with the frequency of 3150 Hz at which we aim to maximize attenuation (figure 4.19). Comparing these results with the unoptimized SDoF liner case (with a resonance frequency different from 3150 Hz), a significant increase in attenuation of an additional 13 dB can be observed (figure 4.20) .

A second optimization, whose results are reported in table 4.4, was carried out by adding σ to the optimization parameters in addition to h and d. This allowed reducing the average SPL from 55.088 to 54.6712. However, this improvement resulted in a significant increase in the computation time, requiring over 50 iterations to meet the stopping criteria (figure 4.21). Observing the values of the various iterations, it is noted that the optimizer,

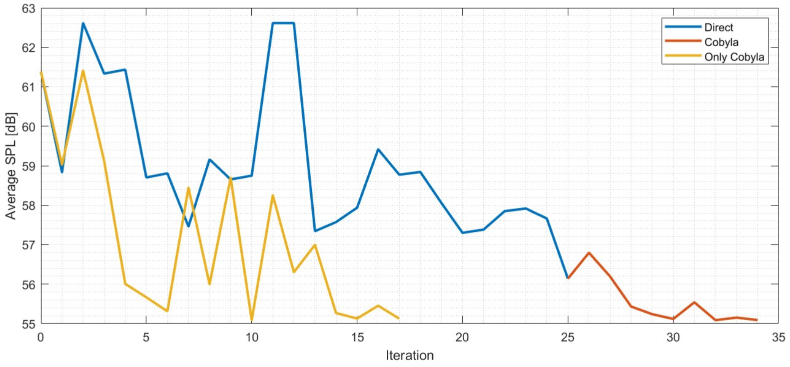

Figure 4.18: SDoF optimization (h, d) iterations without flow

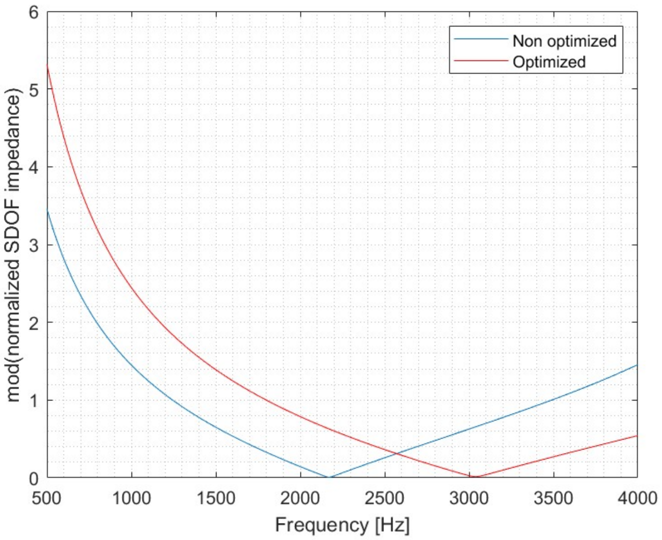

Figure 4.19: Comparison between optimized and non-optimized impedance

Table 4.4: SDoF optimization results, no flow (h, d, σ)

	Direct+Cobyla
h [m]	0.02
d [m]	0.0011
σ [%]	30
Average SPL [dB]	54.6712
Normalized impedance	0.0109 + 0.0443i

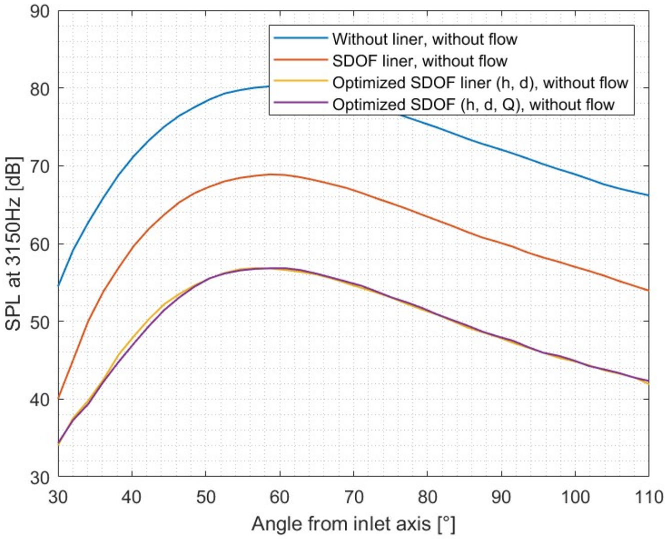

Figure 4.20: Optimization results with SDoF liner

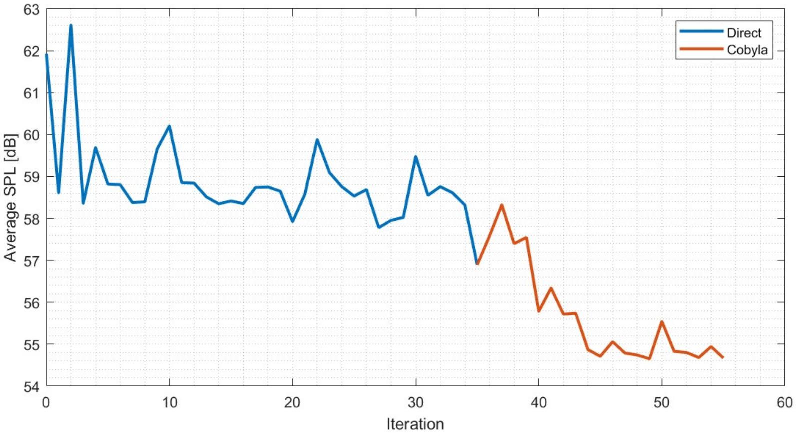

Figure 4.21: SDoF optimization (h, d, Q) iterations without flow

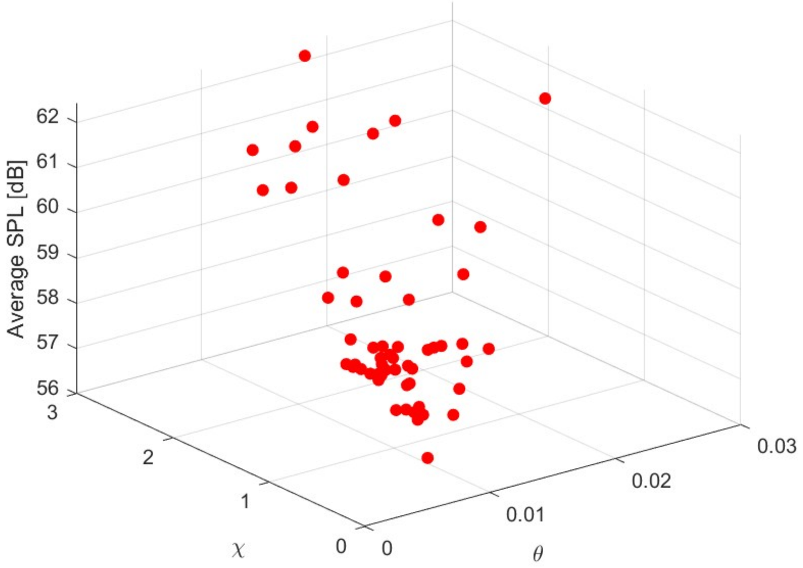

Figure 4.22: Direct SDoF optimization (h,d,Q) values without flow

while moving towards zero reactance, does not explore areas with higher resistance that could guarantee greater attenuation (figure 4.22).

DDoF without flow

The optimization for the DDoF liner, whose results are reported in table 4.5, was carried out by optimizing h_1, h_2, $d1$, and d_2. Following the results during the iterations, it is noticed that even in this case, the optimization algorithm

Table 4.5: DDoF optimization results, no flow

	Direct+Cobyla	Only Cobyla
h_1 [m]	0.0133	0.0176
h_2 [m]	0.02	0.0139
d_1 [m]	0.00097	0.00099
d_2 [m]	0.0012	0.0097
Average SPL [dB]	52.0091	52.5080
Normalized impedance	0.0224 - 0.0513i	0.0166 - 0.0390i

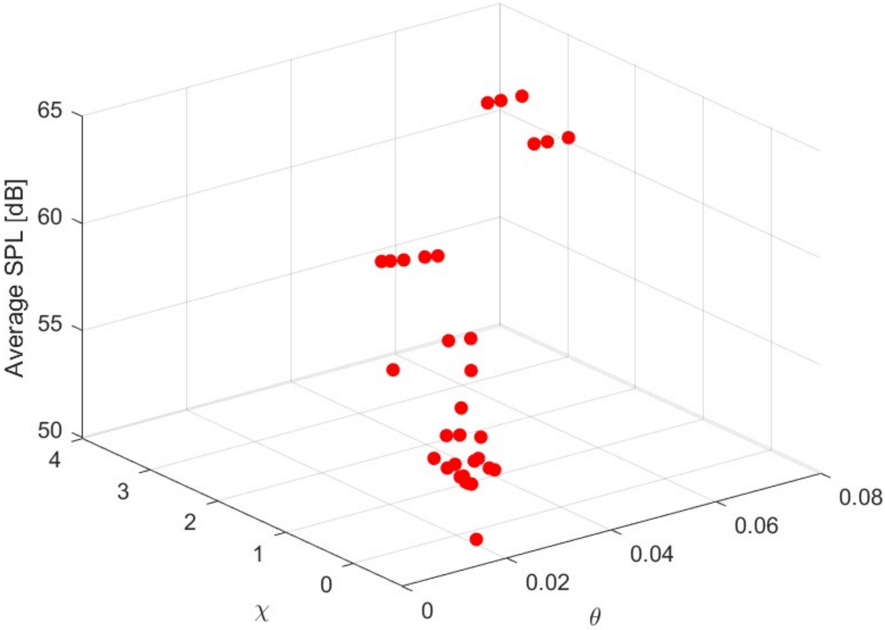

Figure 4.23: Direct DDoF optimization (h_1, d_1, h_2, d_2) values without flow

quickly moves towards resonance conditions (figure 4.23). However, the global optimizer does not seem to explore zones with higher resistance, which could potentially ensure greater attenuation. Also in this case, the optimization approach, which also involves the use of direct methods, leads to much longer computation times, increasing from 20 to 42 iterations (figure 4.24). However, unlike before, going through a global optimization lowers the Average SPL of the optimum by about half a dB, also obtaining different optimization parameter values with the two approaches (table 4.5). It is possible to plot the impedance modulus curve which exhibits two valleys (figure 4.25). Following optimization, one of them coincides with the frequency of 3150Hz (figure 4.26). Comparing the SPL curves for the optimized and non-optimized cases, an increase of over 13dB is observed in this case, resulting in an average SPL of 52.0091 dB, lower than the 54.6712 dB for the SDoF case (figure 4.27).

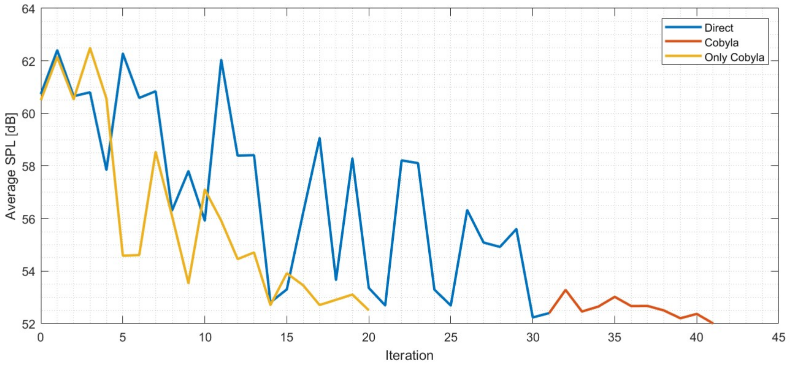

Figure 4.24: DDoF optimization (h_1, d_1, h_2, d_2) iterations without flow

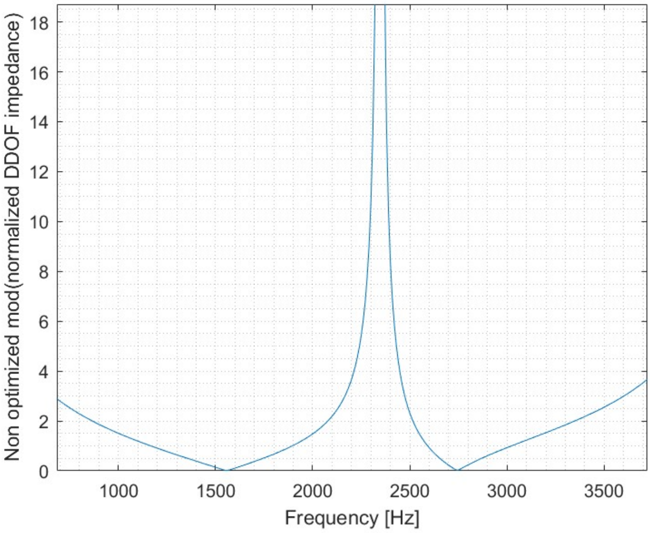

Figure 4.25: Non optimized impedance mod for DDoF liner

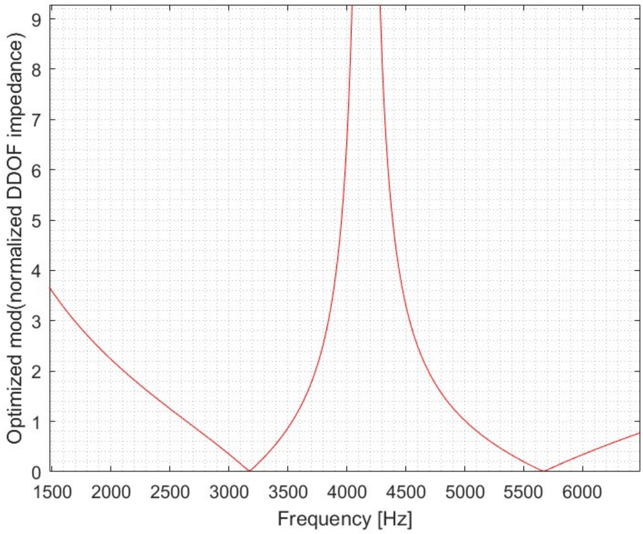

Figure 4.26: Optimized impedance mod for DDoF liner

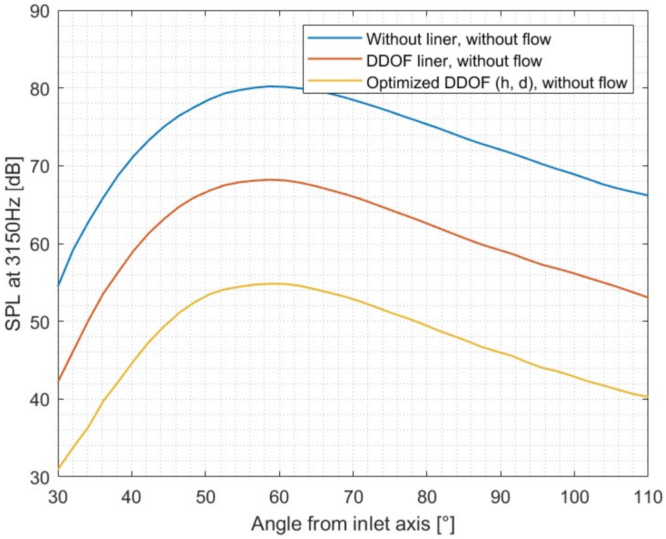

Figure 4.27: Optimization results with DDoF liner

SDoF with flow

By optimizing *h* and *d* for an SDoF liner in the presence of flow (results in table 4.6), it is observed that in this case, the optimization parameters tend towards the same values as they did in the absence of flow. However, what changes significantly are the values of average SPL reached, with reduced attenuation for variable flow and increased attenuation for uniform flow. Again, it can be observed how the variability of the flow determines a variation in the directionality of the noise (figure 4.28), with a maximum shifting towards larger angles relative to the major axis, while uniform flow results in a single translation of the SPL curve towards lower values.The number of iterations required to meet the stopping criteria remains approximately unchanged (figure 4.29 and figure 4.30).

Table 4.6: SDoF optimization results, with flow (h, d)

	Direct+Cobyla, uniform flow	Direct+Cobyla, variable flow
h [m]	0.02	0.0202
d [m]	0.0009	0.000918
σ [%]	0.28 (Non optimized)	0.28 (Non optimized)
Average SPL [dB]	54.1149	52.8133
Normalized impedance	0.0151 + 0.0678i	0.0152 + 0.0678i

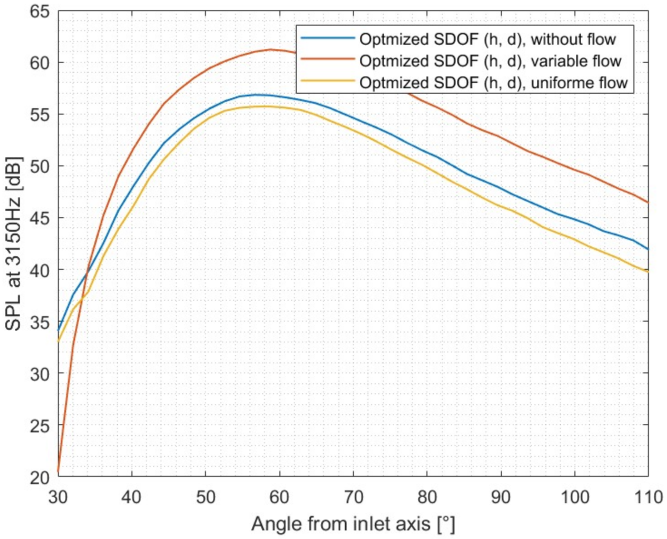

Figure 4.28: Flow effect on the optimization results with SDoF liner

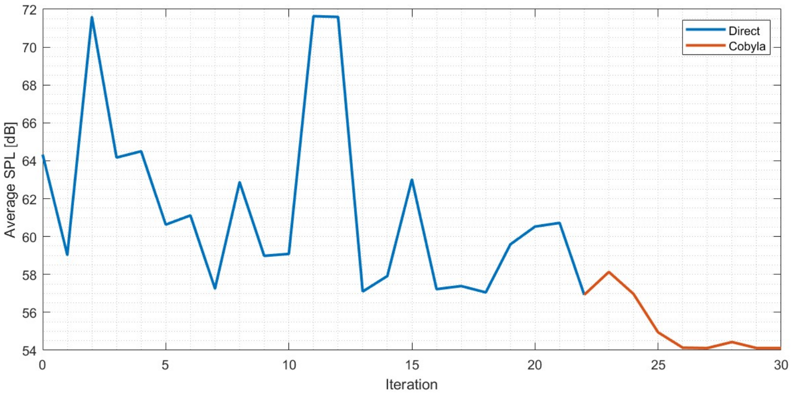

Figure 4.29: SDoF optimization (h, d) iterations with uniforme flow

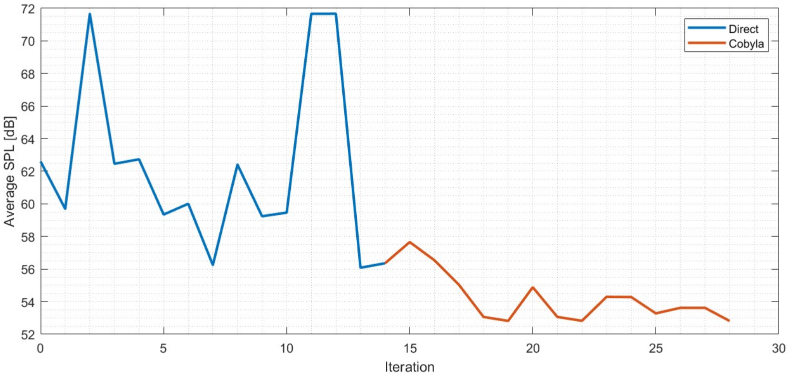

Figure 4.30: SDoF optimization (h,d) iterations with variable flow

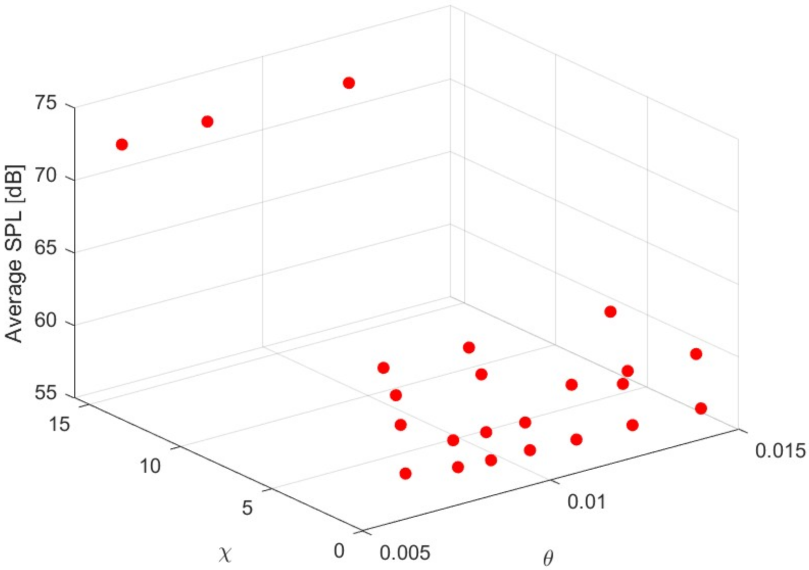

Figure 4.31: Direct SDoF optimization (h,d) values with uniforme flow

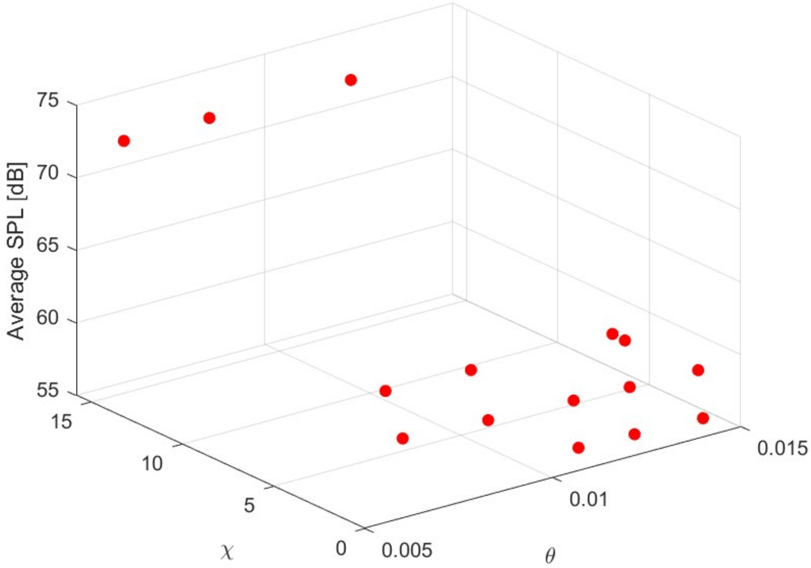

Figure 4.32: Direct SDoF optimization (h,d) values with variable flow

Chapter 5

Conclusions and future developments

In conclusion, this study investigated the optimization of acoustic liners for fan noise attenuation. Initially, analyses were conducted without flow to evaluate the achievable attenuation with non-optimized acoustic treatments, utilizing both SDoF and DDoF liner models. The optimization process involved varying parameters such as cavity depth, thickness, and porosity to minimize the average SPL across multiple microphones.

The results demonstrated significant improvements in attenuation, with optimized liners achieving up to 13 dB of additional reduction compared to non-optimized conditions. The optimization algorithms utilized, including DIRECT and COBYLA, effectively converged towards optimal solutions, although the choice of optimizer and its sequential application impacted computational efficiency. It is concluded that for particularly simple impedance models, choosing a more complex optimization approach is inefficient, but it is preferable to simply use an algorithm that finds the local minimum. However, for more complex models, the choice of initially passing through a global optimizer has proven to be more effective. Therefore, it is advisable to apply more complex approaches to more complex models that can determine a plurality of local minima of acoustic emission. Additionally, in order to increase the complexity of the problem, it is possible to consider additional parameters to further enhance attenuation performance, even pushing towards optimizations with more than 10 parameters. Future research could also explore more sophisticated optimization techniques involving the use of Machine Learning algorithms to speed up the search for the minimum. Moreover, the study investigated the influence of airflow on liner performance. It was found that while flow had minimal impact on attenuation in the absence of liners, the presence of liners exacerbated the effects, with variable flow tending to also alter the directionality of noise emission. Overall, the findings underscore the importance of accurately modeling flow conditions in optimizing acoustic liners, to ensure compliance with regulations. Therefore, future steps could involve applying the code to geometric cases where the real flow field is known, and where the swirl effect at the inlet caused by fan suction is present, in order to compare the results with the simplified resolution of the fluid dynamic field conducted in this thesis. Another aspect to be investigated is how much the results obtained through an axisymmetric simulation differ from a three-dimensional one; the latter would also allow injecting acoustic modes with different azimuthal orders, further complicating the optimization scenario. The simplicity of the analysis is indeed also linked to the fact that only a single mode was injected; further, more advanced analyses could involve optimization in a multimodal case. Finally, experimental validation of optimized liner designs would provide valuable insights for real-world applications in reducing aircraft engine noise.

Appendix A

Python Optimization Code

```python
from numpy import *
from pyfemtown.Command import Optimizer

def myfunc(x,grad):


    ge=optimizer.global_environment
    actran=optimizer.actran
    actranplt=optimizer.actranplt

    dgm_analysis_1 =\
        actran.read_analysis(file='C:file_directory',
        type='ACTRAN', load_topology=True,
        force_modal_components=None)


    h=x[0]
    d=x[1]

    Q=0.28
    f=3150
    c=343
    lunghezza_onda=c/f
    k=2*3.14/lunghezza_onda
    rho=1.225
    mu= 1.716e-5
    tau=0.002
    Cd=0.76
    Z_0=rho*c
```

```

    resistenza_normalizzata=\
    (64*mu*tau)/(2*rho*c*Q*Cd*(d**2))
    reattanza_normalizzata=\
    k*(tau+0.85*d*(1-0.7*(Q**0.5)))/Q-1/math.tan(k*h)

    resistenza= resistenza_normalizzata*Z_0
    reattanza= reattanza_normalizzata*Z_0

    impedenza=complex(resistenza , reattanza)

    admittanza=1/impedenza

    actran.set_prop( actran.get_bc( dgm_analysis_1 ,
        type='Admittance', id=4 ), field=admittanza)
    actran.set_prop(actran.get_output_frf(dgm_analysis_1),
        filename='res.plt')

    actran.run(analysis=dgm_analysis_1 ,
        arguments='--t_max=0.1')

    set_1=actranplt.import_file(file=r'res.13.plt',
        ftype='plt')

    SPL_1=set_1[”POINT_2”, ”1”, ”fp”]
    SPL_2=set_1[”POINT_2”, ”2”, ”fp”]
    SPL_3=set_1[”POINT_2”, ”3”, ”fp”]
    SPL_4=set_1[”POINT_2”, ”4”, ”fp”]
    SPL_5=set_1[”POINT_2”, ”5”, ”fp”]
    SPL_6=set_1[”POINT_2”, ”6”, ”fp”]
    SPL_7=set_1[”POINT_2”, ”7”, ”fp”]
    SPL_8=set_1[”POINT_2”, ”8”, ”fp”]
    SPL_9=set_1[”POINT_2”, ”9”, ”fp”]
    SPL_10=set_1[”POINT_2”, ”10”, ”fp”]

    SPL_11=set_1[”POINT_2”, ”11”, ”fp”]
    SPL_12=set_1[”POINT_2”, ”12”, ”fp”]
    SPL_13=set_1[”POINT_2”, ”13”, ”fp”]
    SPL_14=set_1[”POINT_2”, ”14”, ”fp”]
    SPL_15=set_1[”POINT_2”, ”15”, ”fp”]
    SPL_16=set_1[”POINT_2”, ”16”, ”fp”]
    SPL_17=set_1[”POINT_2”, ”17”, ”fp”]
    SPL_18=set_1[”POINT_2”, ”18”, ”fp”]
    SPL_19=set_1[”POINT_2”, ”19”, ”fp”]
```

```
    SPL_20=set_1[”POINT_2”, ”20”, ”fp”]

    SPL_21=set_1[”POINT_2”, ”21”, ”fp”]
    SPL_22=set_1[”POINT_2”, ”22”, ”fp”]
    SPL_23=set_1[”POINT_2”, ”23”, ”fp”]
    SPL_24=set_1[”POINT_2”, ”24”, ”fp”]
    SPL_25=set_1[”POINT_2”, ”25”, ”fp”]
    SPL_26=set_1[”POINT_2”, ”26”, ”fp”]
    SPL_27=set_1[”POINT_2”, ”27”, ”fp”]
    SPL_28=set_1[”POINT_2”, ”28”, ”fp”]
    SPL_29=set_1[”POINT_2”, ”29”, ”fp”]
    SPL_30=set_1[”POINT_2”, ”30”, ”fp”]

    SPL_31=set_1[”POINT_2”, ”31”, ”fp”]
    SPL_32=set_1[”POINT_2”, ”32”, ”fp”]
    SPL_33=set_1[”POINT_2”, ”33”, ”fp”]
    SPL_34=set_1[”POINT_2”, ”34”, ”fp”]
    SPL_35=set_1[”POINT_2”, ”35”, ”fp”]
    SPL_36=set_1[”POINT_2”, ”36”, ”fp”]
    SPL_37=set_1[”POINT_2”, ”37”, ”fp”]
    SPL_38=set_1[”POINT_2”, ”38”, ”fp”]
    SPL_39=set_1[”POINT_2”, ”39”, ”fp”]
    SPL_40=set_1[”POINT_2”, ”40”, ”fp”]

    SPL_1_Amplitude=abs(SPL_1)
    SPL_2_Amplitude=abs(SPL_2)
    SPL_3_Amplitude=abs(SPL_3)
    SPL_4_Amplitude=abs(SPL_4)
    SPL_5_Amplitude=abs(SPL_5)
    SPL_6_Amplitude=abs(SPL_6)
    SPL_7_Amplitude=abs(SPL_7)
    SPL_8_Amplitude=abs(SPL_8)
    SPL_9_Amplitude=abs(SPL_9)
    SPL_10_Amplitude=abs(SPL_10)

    SPL_11_Amplitude=abs(SPL_11)
    SPL_12_Amplitude=abs(SPL_12)
    SPL_13_Amplitude=abs(SPL_13)
    SPL_14_Amplitude=abs(SPL_14)
    SPL_15_Amplitude=abs(SPL_15)
    SPL_16_Amplitude=abs(SPL_16)
    SPL_17_Amplitude=abs(SPL_17)
    SPL_18_Amplitude=abs(SPL_18)
    SPL_19_Amplitude=abs(SPL_19)
```

```
    SPL_20_Amplitude=abs(SPL_20)

    SPL_21_Amplitude=abs(SPL_21)
    SPL_22_Amplitude=abs(SPL_22)
    SPL_23_Amplitude=abs(SPL_23)
    SPL_24_Amplitude=abs(SPL_24)
    SPL_25_Amplitude=abs(SPL_25)
    SPL_26_Amplitude=abs(SPL_26)
    SPL_27_Amplitude=abs(SPL_27)
    SPL_28_Amplitude=abs(SPL_28)
    SPL_29_Amplitude=abs(SPL_29)
    SPL_30_Amplitude=abs(SPL_30)

    SPL_31_Amplitude=abs(SPL_31)
    SPL_32_Amplitude=abs(SPL_32)
    SPL_33_Amplitude=abs(SPL_33)
    SPL_34_Amplitude=abs(SPL_34)
    SPL_35_Amplitude=abs(SPL_35)
    SPL_36_Amplitude=abs(SPL_36)
    SPL_37_Amplitude=abs(SPL_37)
    SPL_38_Amplitude=abs(SPL_38)
    SPL_39_Amplitude=abs(SPL_39)
    SPL_40_Amplitude=abs(SPL_40)

    SPL_1_dB=20 * math.log10( SPL_1_Amplitude / (2e-5))
    SPL_2_dB=20 * math.log10( SPL_2_Amplitude / (2e-5))
    SPL_3_dB=20 * math.log10( SPL_3_Amplitude / (2e-5))
    SPL_4_dB=20 * math.log10( SPL_4_Amplitude / (2e-5))
    SPL_5_dB=20 * math.log10( SPL_5_Amplitude / (2e-5))
    SPL_6_dB=20 * math.log10( SPL_6_Amplitude / (2e-5))
    SPL_7_dB=20 * math.log10( SPL_7_Amplitude / (2e-5))
    SPL_8_dB=20 * math.log10( SPL_8_Amplitude / (2e-5))
    SPL_9_dB=20 * math.log10( SPL_9_Amplitude / (2e-5))
    SPL_10_dB=20 * math.log10( SPL_10_Amplitude / (2e-5))

    SPL_11_dB=20 * math.log10( SPL_11_Amplitude / (2e-5))
    SPL_12_dB=20 * math.log10( SPL_12_Amplitude / (2e-5))
    SPL_13_dB=20 * math.log10( SPL_13_Amplitude / (2e-5))
    SPL_14_dB=20 * math.log10( SPL_14_Amplitude / (2e-5))
    SPL_15_dB=20 * math.log10( SPL_15_Amplitude / (2e-5))
    SPL_16_dB=20 * math.log10( SPL_16_Amplitude / (2e-5))
    SPL_17_dB=20 * math.log10( SPL_17_Amplitude / (2e-5))
    SPL_18_dB=20 * math.log10( SPL_18_Amplitude / (2e-5))
    SPL_19_dB=20 * math.log10( SPL_19_Amplitude / (2e-5))
```

```
    SPL_20_dB=20 * math.log10( SPL_20_Amplitude / (2e-5))

    SPL_21_dB=20 * math.log10( SPL_21_Amplitude / (2e-5))
    SPL_22_dB=20 * math.log10( SPL_22_Amplitude / (2e-5))
    SPL_23_dB=20 * math.log10( SPL_23_Amplitude / (2e-5))
    SPL_24_dB=20 * math.log10( SPL_24_Amplitude / (2e-5))
    SPL_25_dB=20 * math.log10( SPL_25_Amplitude / (2e-5))
    SPL_26_dB=20 * math.log10( SPL_26_Amplitude / (2e-5))
    SPL_27_dB=20 * math.log10( SPL_27_Amplitude / (2e-5))
    SPL_28_dB=20 * math.log10( SPL_28_Amplitude / (2e-5))
    SPL_29_dB=20 * math.log10( SPL_29_Amplitude / (2e-5))
    SPL_30_dB=20 * math.log10( SPL_30_Amplitude / (2e-5))

    SPL_31_dB=20 * math.log10( SPL_31_Amplitude / (2e-5))
    SPL_32_dB=20 * math.log10( SPL_32_Amplitude / (2e-5))
    SPL_33_dB=20 * math.log10( SPL_33_Amplitude / (2e-5))
    SPL_34_dB=20 * math.log10( SPL_34_Amplitude / (2e-5))
    SPL_35_dB=20 * math.log10( SPL_35_Amplitude / (2e-5))
    SPL_36_dB=20 * math.log10( SPL_36_Amplitude / (2e-5))
    SPL_37_dB=20 * math.log10( SPL_37_Amplitude / (2e-5))
    SPL_38_dB=20 * math.log10( SPL_38_Amplitude / (2e-5))
    SPL_39_dB=20 * math.log10( SPL_39_Amplitude / (2e-5))
    SPL_40_dB=20 * math.log10( SPL_40_Amplitude / (2e-5))


    OSPL=(SPL_1_dB+...+SPL_40_dB)/40

    obj_func=OSPL


    ge.report_file.write(str(ge.iteration)+' '+str(x[0])+' '+str(x[1])+' '+str(obj_func)+' \n')
    ge.report_file.flush()
    ge.iteration +=1

    optimizer.clear_all()

    return obj_func

def main() :

    opt=optimizer.optimizer(optimizer.GN_DIRECT,2)

    optimizer.global_environment.iteration=0
```

```
    optimizer.global_environment.report_file=\
    optimizer.openfile('output.dat','w')

    opt.set_min_objective(myfunc)
    opt.set_lower_bounds([0.02, 0.0009])
    opt.set_upper_bounds([0.06, 0.0015])
    opt.set_xtol_rel(1e-1)

    x=opt.optimize([0.03, 0.0013])

    minf=opt.last_optimum_value()
    optimizer.message("Total numer of iteration:
       %d"%(optimizer.global_environment.iteration-1))
    optimizer.message("Optimum at %s" %str(x))
    optimizer.message("Minimum value= %g" %minf)
    optimizer.message("Result code = %g"
       %opt.last_optimize_result())

optimizer=Optimizer()
main()
```

Listing A.1: Python optimization code for SDoF liner

Bibliography

[1] *Actran 2023.1. User's Guide ActranDGM: Theory, Input File Syntax and Computation Process*. Hexagon, FFT. 2023.

[2] *Actran DGM - Introduction to Actran DGM*. Hexagon, FFT. 2019.

[3] *Actran DGM - Non convected DGM simulations*. Hexagon, FFT. 2019.

[4] *Actran DGM - Turbomachine exhaust simulation*. Hexagon, FFT. 2019.

[5] Renzo Arina. *Lecture Notes on Aeroacoustic*. Politecnico di Torino. 2023.

[6] Beck and Benjamin S. 'Grazing incidence modeling of a metamaterial-inspired dual-resonance acoustic liner'. In: *Health Monitoring of Structural and Biological Systems* (2014). DOI: 10.1117/12.2059834.

[7] Gijs Bouman. 'Aeroacoustic response of an acoustic liner'. In: *Delft University of Technology* (2021).

[8] BRUIT-PARIF. 'Health impact of transport noise in the densely populated zone of Ilede-France region'. In: (2019).

[9] C. Bailly C. Bogey and D. Juve. 'On the discrete and continuous spectrum of acoustic-vortical waves'. In: *AIAA Journal* (2002). DOI: https://doi.org/10.1260/1475-472X.12.7-8.743.

[10] Damiano Casalino and Mattia Barbarino. 'Optimization of a Single Slotted Lined Flap for Airframe Noise Reduction'. In: June 2011. ISBN: 978-1-60086-943-3. DOI: 10.2514/6.2011-2730.

[11] Damiano Casalino, Andreas Hazir and Adrien Mann. 'Turbofan Broadband Noise Prediction Using the Lattice Boltzmann Method'. In: *AIAA Journal* 56 (Sept. 2017). DOI: 10.2514/1.J055674.

[12] Geng Deng and Michael C. Ferris. 'Extension of the direct optimization algorithm for noisy functions'. In: *2007 Winter Simulation Conference*. 2007, pp. 497–504. DOI: `10.1109/WSC.2007.4419640`.

[13] Giuseppe Dilillo. 'Design and Optimization of Acoustic Liners with Complex Cavities for Improved Broadband Noise Absorption'. PhD thesis. Politecnico di Milano, 2020.

[14] Giuseppe Dilillo, Paul Murray and Massimiliano Giulio. 'Impact of the engine fan source and wall boundary layer on inlet liner design'. In: (June 2022). DOI: `10.2514/6.2022-2964`.

[15] Giuseppe Dilillo, Paul Murray and Massimiliano Di Giulio. 'Improved aero engine inlet attenuation from novel broadband liners'. In: *28th AIAA/CEAS Aeroacoustics 2022 Conference* (2022). DOI: `https://doi.org/10.2514/6.2022-2965`.

[16] F. Fahy. 'Foundations of Engineering Acoustics'. In: *Academic Press - Elsevier Science* (2001).

[17] Damiano Casalino Francesco Avallone. 'Acoustic-induced velocity in a multi-orifice acoustic liner grazed by a turbulent boundary layer'. In: *American Institute of Aeronautics and Astronautics (AIAA)* (2021). DOI: `https://doi.org/10.2514/6.2021-2169`.

[18] Lorenzo Garibaldi. 'Eurocargo CNG E6 Exhaust System: Acoustic Simulation and SNGR Approach by ACTRAN'. In: *Polytechnic of Turin* (2021).

[19] S. Giaccherini et al. 'Validation of an Analytical Model for the Acoustic Impedance Eduction of Multicavity Resonant Liners by a High-Fidelity Large Eddy Simulation Approach'. In: *Journal of Turbomachinery* 145.8 (2023), p. 081002. DOI: `10.1115/1.4056984`.

[20] Simone Giaccherini et al. 'Validation of an Analytical Model for the Acoustic Impedance Eduction of Multicavity Resonant Liners by a High-Fidelity Large Eddy Simulation Approach'. In: *Journal of Turbomachinery* 145.8 (Apr. 2023), p. 081002. DOI: `10.1115/1.4056984`.

[21] Stewart Glegg and William Devenport. *Aeroacoustics of Low Mach Number Flows. Chapter 18: Fan noise*. Academic Press, 2017.

[22] Nicola Gravagnone, Paul Murray and Massimiliano Giulio. 'Optimisation of non-locally reacting liners for improved duct attenuation'. In: (June 2022). DOI: `10.2514/6.2022-2931`.

[23] *HandWiki-Optimization algorithms and methods: COBYLA*. URL: `https://handwiki.org/wiki/COBYLA`.

[24] D. R. Jones, C. D. Perttunen and B. E. Stuckman. 'Lipschitzian optimization without the Lipschitz constant'. In: *Journal of Optimization Theory and Applications* 79 (1993), pp. 157–181. DOI: `10.1007/bf00941892`.

[25] Michael Jones, Brian Howerton and Earl Ayle. 'Evaluation of Parallel-Element, Variable-Impedance, Broadband Acoustic Liner Concepts'. In: June 2012. ISBN: 978-1-60086-932-7. DOI: `10.2514/6.2012-2194`.

[26] S.J. Horowitz K.J. Baumeister. 'Finite element integral simulation of static and flight fan noise radiation from the JT15D turbofan engine'. In: *NASA Technical Reports Server* (1982).

[27] E. J. Rice L. J. Heidelberg and L. Homyak. 'Acoustic Performance of Inlet Suppressors on an Engine Generating a Single Mode'. In: *AIAA Paper 81-1965* (1981).

[28] E. J. Rice L. J. Heidelberg and L. Homyak. 'ExperimentalEvaluation 1of a Spinning Mode Acoustic Treatment Design Concept for Aircraft Inlets'. In: *AIAA Paper 81-1965* (1980).

[29] XuQuiang Ma and ZhengTao Su. 'Development of acoustic liner in aero engine: a review'. In: *Science China Technological Sciences* 63 (2020), pp. 2491–2504. DOI: `https://doi.org/10.1007/s11431-019-1501-3`.

[30] Bruno Mangin. 'Modelling acoustic propagation in modern turbofan intakes using a multimodalmethod'. In: *Le Mans Université* (2023).

[31] Lars-Erik Eriksson Mattias Billson and Lars Davidson. 'Computation of flow noise using source terms in linearized euler's equations'. In: *AIAA Journal* (2005). DOI: `https://doi.org/10.2514/2.1665`.

[32] R. E. Motsinger and R. E. Kraft. *“Design and Performance of Duct Acoustic Treatment”, Aeroacoustics of Flight Vehicles: Theory and Practice, Volume 2: Noise Control*. Edited by H. H. Hubbard, NASA Langley Research Center, Hampton, VA, 1991.

[33] Paul Murray and R.J. Astley. ‘Development of a single degree of freedom perforate impedance model under grazing flow and high SPL’. In: *18th AIAA/CEAS Aeroacoustics Conference* (May 2012). DOI: `10.2514/6.2012-2294`.

[34] Suresh Palani et al. ‘Assessment of novel acoustic liners for aero-engine applications with sheared mean flow’. In: (2022). DOI: `10.2514/6.2022-2900`.

[35] L. M. Pereira et al. ‘Lattice-Boltzmann Numerical Investigation of a Realistic Multi-Cavity Acoustic Liner with Grazing Flow’. In: *AIAA/CEAS Aeroacoustics 2022 Conference* (2022). DOI: `https://doi.org/10.2514/6.2022-2967`.

[36] M. J. D. Powell. ‘A direct search optimization method that models the objective and constraint functions by linear interpolation’. In: *Advances in Optimization and Numerical Analysis*. Ed. by S. Gomez and J.-P. Hennart. Vol. 275. Mathematics and Its Applications. Springer, 1994, pp. 51–67. DOI: `10.1007/978-94-015-8330-5_4`.

[37] Rie Sugimoto, Paul Murray and R.J. Astley. ‘Folded Cavity Liners for Turbofan Engine Intakes’. In: June 2012. ISBN: 978-1-60086-932-7. DOI: `10.2514/6.2012-2291`.

[38] Daniel Sutliff. ‘Rotating rake turbofan duct mode measurement system’. In: *The Journal of the Acoustical Society of America* 118 (Oct. 2005). DOI: `10.1121/1.4779000`.

[39] E. Edmane T. Christopher P. Sarah. ‘Physics of Acoustic Radiation from Jet Engine Inlets’. In: *18th AIAA/CEAS Aeroacoustics Conference* (2012). DOI: `10.2514/6.2012-2242`.

[40] Ju H. Tam C. K. and Walker B. E. ‘Numerical simulation of a slit resonator in a grazing flow under acoustic excitation’. In: *Journal of Sound and Vibration, Vol. 313, pp. 449–471* (2008). DOI: `https://doi.org/10.1016/j.jsv.2007.12.018`.

[41] C. Bailly W. Bechara and P. Lafon. 'Acoustic source terms for the linearized euler equations in conservative form'. In: *AIAA Journal* (1994). DOI: `https://doi.org/10.2514/1.12858`.

[42] J. Winkler et al. 'High fidelity modeling tools for engine liner design and screening of advanced concepts'. In: *International Journal of Aeroacoustics* 20 (5-7) (2021), pp. 530–560. DOI: `https://doi.org/10.1177/1475472X211023884`.

[43] T Zandbergen. 'Do Locally Reacting Acoustic Liners Always Behave as They Should?' In: *AIAA Journal* 18.4 (2012). DOI: `https://doi.org/10.2514/3.50771`.

[44] Qi Zhang and Daniel J. Bodony. 'Numerical investigation of a honeycomb liner grazed by laminar and turbulent boundary layers'. In: *Journal of Fluid Mechanics* 792 (2016), pp. 936–980. DOI: `10.1017/jfm.2016.79`.